$1 - G(Q)$ is a factor which reduces the cross section at small momentum transfer due to the Pauli exclusion principle, and $\frac{d\sigma_H}{d\Omega}$ is the η,η' photoproduction cross section on a single nucleon. The relative phase between the Primakoff and nuclear coherent amplitudes without final state interactions is given by ϕ_1 and the phase shift of the outgoing meson due to final state interactions in the final state is given by ϕ_2.

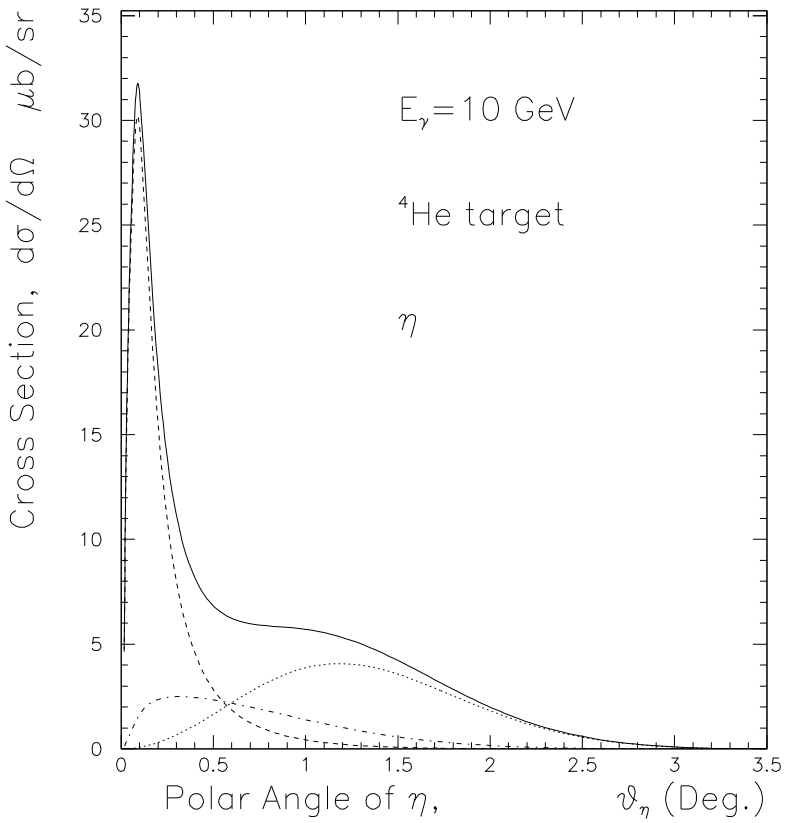

Figure 4: Differential cross sections (electromagnetic and nuclear) for the $\gamma + {}^4He \rightarrow \eta + {}^4He$ reaction at small angles at 10 GeV. The solid line is the total differential cross section from all the process, the dashed line is from Primakoff process, the dotted line is from the nuclear coherent process, and the dot-dash line is from the interference of the Primakoff and nuclear coherent processes.

Kinematical considerations enable one to separate Primakoff from other photo-meson production mechanisms. The Primakoff cross section is zero for mesons emitted along the incident photon direction (minimum four-momentum transfer t to the recoiling nucleus),

has a sharp maximum at a very small angle (small t), and falls rapidly to zero at larger angles. It is proportional to Z^2, and its peak value is roughly proportional to E^4. The nuclear coherent cross section for spin zero nuclei is also zero in the forward direction, but has a broad maximum outside the angular region of the Primakoff effect, and falls at larger angles as shown in figure 4, where the amplitudes are normalized to the Cornell data[2]. The angular dependence (or t dependence) of the Primakoff signal and the background are different, allowing $\Gamma(\eta \rightarrow \gamma\gamma)$ and $\Gamma(\eta' \rightarrow \gamma\gamma)$ to be extracted from a fit to the angular distribution (or t distribution) of the photoproduced mesons. Measurements of the nuclear effects at larger angles are necessary to determine the unknown parameters in the production mechanism and thus make an empirical determination of the nuclear contribution in the Primakoff peak region. Consequently, to study the 2γ decay width of η and η' requires good angular resolution on the meson production angle, or good t resolution on the recoiling nucleus, to eliminate nuclear coherent production background.

Figure 5 shows t, the square of the four-momentum transferred to the nucleus, as a function of the meson production angles for the π^0, η and η'. The arrows indicate the locations of the Primakoff peaks. As one can see for the π^o, the Primakoff cross section is peaked at a very small t ($\sim 10^{-6}\ GeV^2$), so that the recoiling nucleus is likely to stay in the ground state. As the mass of the η and η' are higher than that of the π^0 however, the Primakoff cross sections are peaked at higher t (a few times $10^{-4}\ GeV^2$ for η and 10^{-3} GeV^2 for η'). As such, it becomes necessary to check the coherency of the meson production, especially for the case of the η'. A serious drawback of the previous Primakoff experiment[2] on $\Gamma(\eta \rightarrow \gamma\gamma)$ is that coherency was not established. As a result, recoil detection is required to ensure coherency and thereby distinguish backgrounds. In addition, as indicated in the previous section, in all the existing $\Gamma(\eta' \rightarrow \gamma\gamma)$ measurements, the signature of η' production is reconstructed by registering the decay particles from the η'. Consequently, poor knowledge of η' branching ratios ($\sim 5\%$) will limit the precision of the measurement. By tagging the η' through detection of the recoiling nucleus this uncertainty can be avoided.

As we are going to use the recoil detection technique, the target thickness must be thin enough to allow the recoiling nuclei to exit from the target. For such a thin target, tagging virtual photons at 0° represents a big advantage over real photon tagging because of the higher photon flux. Therefore, we propose using tagged zero degree virtual photons in the $\Gamma(\eta \rightarrow \gamma\gamma)$ and $\Gamma(\eta' \rightarrow \gamma\gamma)$ measurements.

The cross sections for the Primakoff effect to produce the η on ^4He is presented in figure 4. Compared to the Primakoff effect to produce the π^0, the η production has a significantly smaller cross section and peaks at relatively larger production angles. This is a consequence of the much larger mass of the η which significantly increases the momentum transfer at a given production angle. As a result the Primakoff peak is harder to distinguish from the nuclear coherent peak. There are two ways to ameliorate this problem. One is to go to higher photon energies, which will help separate the Primakoff signal from the background by pushing the Primakoff peak to the smaller angles and increase the Primakoff cross section ($\sigma_P \propto E^4$). As such, the proposed 11 GeV upgrade to the CEBAF accelerator is vital to

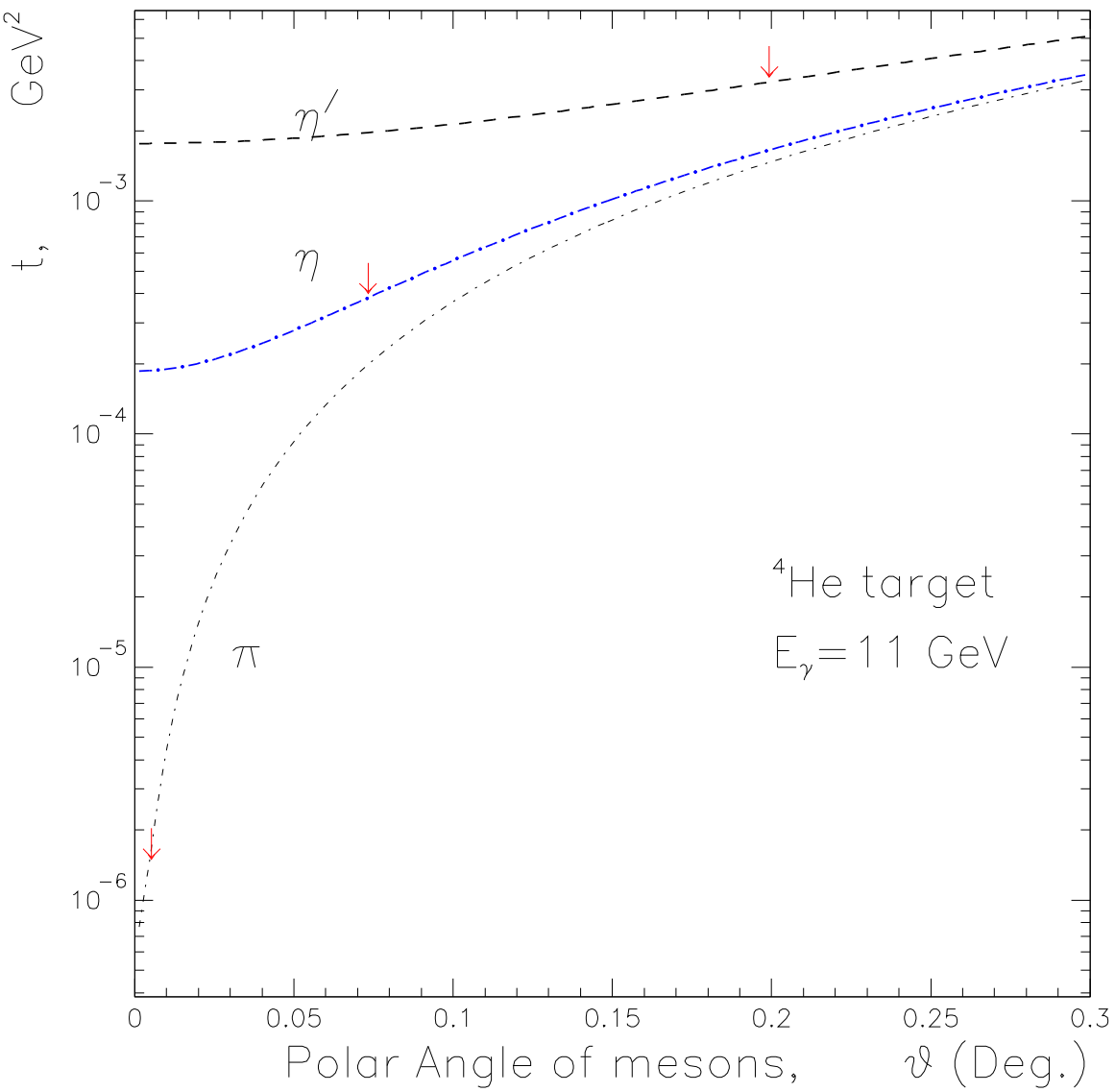

Figure 5: The four-momentum transfer to the nucleus t as a function of the meson production angles of π^0,η and η'. The arrows indicates the location of Primakoff peaks.

these measurements. Another improvement is to use lighter targets such as ^1H, ^4He or ^{12}C, which are more stable compared to heavier nuclei, thereby enhancing coherency. We argue that by simultaneously going to higher photon energies and using lighter Primakoff production targets, one can make clean measurements of the widths.

3.3 Experimental Setup for η/η' Width Measurement

We propose to use the virtual photon tagging technique to produce the η/η' mesons, and to detect multiphoton final states in a hybrid calorimeter. In addition to the 11 GeV upgrade to the CEBAF accelerator, such measurements would require (1), a magnetic spectrometer for the virtual photon tagging system, (2), a low energy recoil detector based on low pressure multiwire proportional chambers to enable the separation of photoproduction via the Primakoff mechanism from other processes, and to identify the formation of mesons from missing mass reconstruction, (3) a $1.5m \times 1.5m$ multichannel hybrid calorimeter consisting of lead glass Cherenkov counters and a high resolution insertion in the central region composed of lead tungstate scintillating blocks, to detect decay particles from the meson decay, and (4), a small angle detector to enable the rejection of Møller and elastically scattered electrons. (see figure 6). The details of each instrument will be described below.

3.3.1 Zero Degree Virtual Photon Tagging System

In order to detect low energy recoiling nuclei from the target, very thin ($\sim 10^{-5}$ radiation length) targets are required. In this case, the virtual photon tagging technique holds a big advantage over real photon tagging. This is because, for the same electron tagging rate, the the ratio of the counting rate between the zero degree virtual photon tagger and the real photon tagger is given by[14]

$$\frac{R_{(0^0 e,e'x)}}{R_{(tagged-\gamma,x)}} = \frac{t^V + t/2}{t} \tag{13}$$

where t^V is an effective virtual photon target thickness (~ 0.02), and t is the real photon target thickness. For a $\sim 10^{-5}$ radiation length of target,

$$\frac{R_{(0^0 e,e'x)}}{R_{(tagged-\gamma,x)}} \sim \frac{0.02 + 10^{-5}}{10^{-5}} \sim 10^3 \tag{14}$$

which indicates that the virtual photon rate is about 10^3 times larger than real photon rate, while maintaining the signal to noise ratio at the same magnitude for the both virtual and real photon cases[14]. As pointed out by Hyde-Wright *et. al*[14], the signal to noise ratio will be optimized by operating near the bremsstrahlung endpoint, which will be the case in our experiment. The rates of the zero degree virtual photon tagging experiment will be limited by the electron singles rate in the electron spectrometer arm, which is dominated by the electrons from the bremsstrahlung process rather than by the reaction of interest.

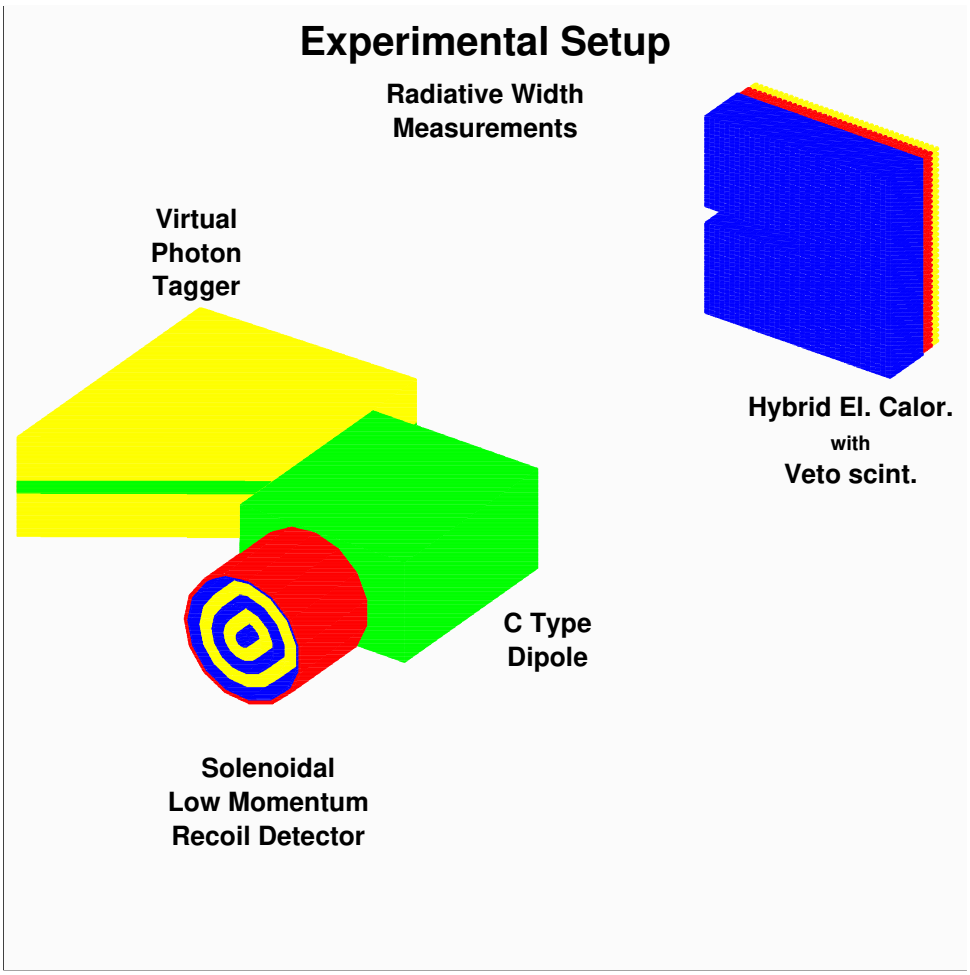

Figure 6: Experimental setup for η and η' two–gamma decay width measurements. It includes (1) a magnetic spectrometer for the virtual photon tagging system, (2), a low energy recoil detector.(3) a $1.5m \times 1.5m$ multichannel hybrid calorimeter, (4), a small angle detector at far downstream of the target, which is not shown in the figure,(5), a C type dipole magnet to separate the scattering electrons from the primary electron beam.

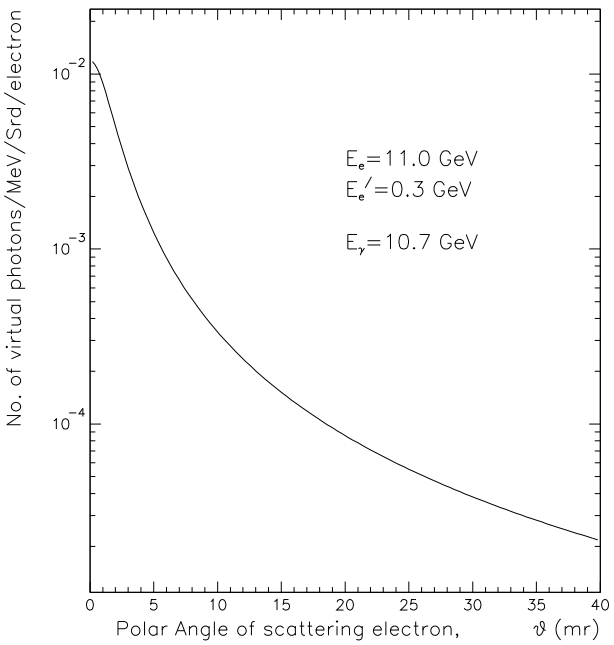

Figure 7: Calculated photon flux factor angular distribution.

The virtual photon flux factor Γ, which is the virtual number of virtual photons radiated per unit photon energy per unit electron solid angle per incident electron is[14]:

$$\begin{aligned}\Gamma(e_1,\omega,\theta) &= \frac{\alpha}{4\pi^2\omega}[\frac{e_1^2+e_2^2}{2e_1^2}(\frac{m^2\omega^2}{4e_1^2e_2^2}+sin^2(\frac{\theta}{2}))^{-1}-\frac{e_2m^2\omega^2}{e_14e_1^2e_2^2}(\frac{m^2\omega^2}{4e_1^2e_2^2}+sin^2(\frac{\theta}{2}))^{-2} \\ &\quad -\frac{(e_1+e_2)^2}{4e_1^2}(\frac{\omega^2}{4e_1e_2}+sin^2(\frac{\theta}{2}))^{-1}] \qquad (15)\end{aligned}$$

where e_1 and e_2 are the incident and scattered electron energies, θ is scattering angle, ω is photon energy, m is electron mass.

For an 11 GeV electron beam and 10.7 GeV tagged virtual photons, the flux factor distribution is shown in figure 7. It can be seen that the virtual photons are mostly in the forward direction, and the intensity of photons falls rapidly with the scattering angle.

We can use an existing spectrometer at TJNAF as a zero degree virtual photon tagger. One such example is the Enge spectrometer, which was used to tag zero degree virtual photons in an HNSS hypernuclear spectroscopy experiment (Mar 1–May 14, 2000) and has proved to be successful. The spectrometer is a split pole magnet[16]. Its resolution without correction for the angle-position correlation is about 3×10^{-4}, so that only a focal plane detector package, a silicon strip detector and a segmented scintillator detector were used during the HNSS experiment for timing and particle identification as well as position determination. In the Primakoff experiment, we will monitor the virtual photon flux by the electron scattering angle. Therefore, another off focal plane detector is needed in order to measure the electron scattering angle. During the HNSS experiment, the Enge spectrometer proved to be capable of running at electron singles rates of up to 2×10^8/sec, which is much higher than our requirement ($\sim 7 \times 10^6$/sec).

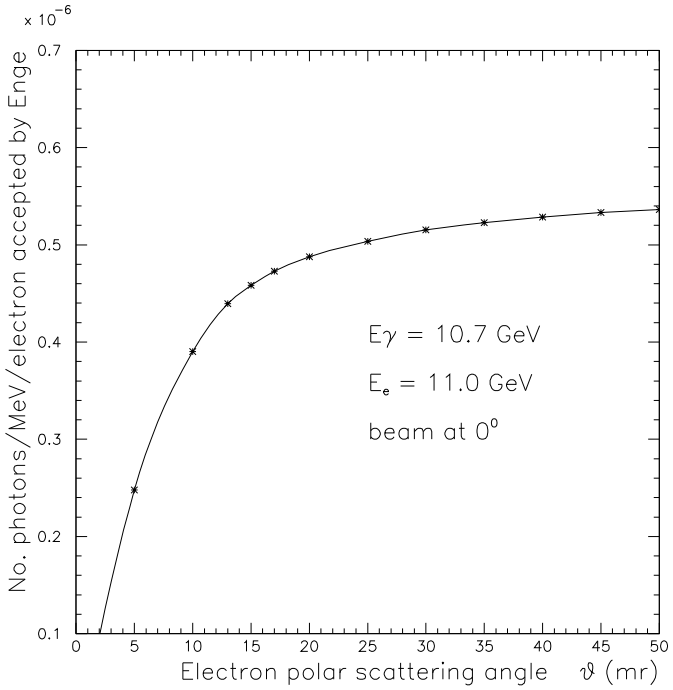

Figure 8: The photon flux distribution registered by the Enge acceptance.

Figure 8 shows the photon flux distribution after passing through the Enge spectrometer acceptance, which was simulated by RAYTRACE [17]. It indicates that we may control the photon flux to better than 1% if the angular resolution at the focal plane is better than a few mr.

As the Enge spectrometer angular acceptance is relatively small (1.6 msr), we are also keeping open the option to use another electron spectrometer which has a larger acceptance, so that we will be not sensitive to the spectrometer offsets.

3.3.2 Low-Energy Recoil Detection

a.)**Importance of Low-Energy Recoil Detection**

Detection of recoiling nuclei can offer important kinematical constraints on the reaction. Low-energy recoil measurements in Primakoff experiments performed in conjunction with measurements of the forward system allow one to:

- Separate the coherent process from incoherent background;
- Determine the four-momentum transfer to the nucleus (t) with high precision;

- Exclusively identify the formation of the mesons without detecting their decay particles.

A crucial parameter in the Primakoff process is the square of the invariant four-momentum, t, defined as

$$t = (p_o - p_i)^2 = (p_r - p_t)^2 \tag{16}$$

where p_i is the momentum of incident photon, p_o is the momentum of the outgoing meson (η or η'), p_t is the momentum of the target particle, and p_r is the momentum of the recoil nucleus. Assuming that the target is at rest ($p_t = 0$), in a coherent process ($m_r = m_t = M$), one obtains from the above definition:

$$t = (p_r - p_t)^2 = -2MT, \tag{17}$$

where T is the recoiling nucleus' kinetic energy. Therefore the measurement error will be determined by:

$$\delta t = 2M \cdot \delta T \tag{18}$$

which shows that error in t is determined only by the uncertainty of T. Comparing this with the measurement of t from the forward angle spectrometer in the elastic process, at small scattering angles θ_o, t can be approximated by

$$-t \sim p_i^2 \cdot \theta_o^2, \tag{19}$$

For a known incident momentum p_i, the error in t is:

$$\delta t \sim 2p_i^2 \cdot \theta_o \cdot \delta\theta_o, \tag{20}$$

As one can see, t is determined by the error in the forward scattering angle, and is also proportional to p_i^2. When the incident momentum p_i increases, the error, δt, grows as well. As a result, determining the t through the recoil measurement has an advantage over measuring the forward scattering angle. As mentioned earlier, the recoil detection technique is also the only way to reach a measurement error of less than 5% in the case of the η' because of the poor knowledge of the η' decay branching ratio ($\sim 5\%$).

As the kinetic energy of the recoiling nucleus is low, a thin target is very important to allow recoiling nuclei to exit the target. Therefore one needs an intense beam to have a good production rate. As a result, the recoil detectors must have the ability to work in a high radiation environment. The properties of Low-Pressure Multiwire Proportional Chambers (LPMWPCs) and Low-Pressure Multi-Step Chambers (LPMSCs)[19][20] are appropriate to these goals. The main features of such chambers are summarized below:

- High rate capability ($\sim 10^5 Hz/mm^2$);
- Extreme insensitivity to gamma and neutron backgrounds;

- Capability to operate from an external gate, allowing the minimization of space charge effects;
- Negligible radiation damage;
- Good timing resolution ($\sim$ 200 ps, FWHM for fission fragments);
- Good position resolution ($\sim 200\mu m$, FWHM)
- High efficiency ($\sim 100\%$) for detecting low energy recoils;
- Negligible influence on the energy of recoils (the recoiling nucleus travels through the detectors with practically constant velocity).

b.) **Scientific Evaluation of the Low Pressure Chamber Technique**

During the past four years, a member of our collaboration (A. Margaryan) has been leading a group to develop LPMWPCs for a time-zero fission fragment (FF) detector for the direct measurement of the heavy hypernuclei lifetime at Jefferson Lab. The detector's characteristics and the method of time-zero reconstruction were investigated using fission fragments from a Cf-252 spontaneous fission source. It was shown that heptane, hexane, and isobutane gases at a pressure of 1-3 Torr are all suitable for such a fission fragment detector. As desired by experiment E95-002 (E99-003) [21], a timing and position resolution of about 200ps (FWHM) and 800μm (FWHM) for a chamber size of 21×21 cm^2 was achieved. In order to test the influence of the high radiation on the operation of the fission fragment detector, it was put in Hall C during E96-003 and E91-007 experiments near the beam at 7°, 20 meters downstream from a 4% radiator and a 12 cm liquid deuterium target. There were no noticeable changes in timing resolution of the detectors up to 10μA electron beam current, which produces 10^9 electrons/second in the solid angle of the chamber according to a Monte Carlo simulation[22]. At higher intensities (40-70 μA), the signals decreased 2-3 times due to space charge effects, but the time resolution of fission fragments from a Cf-252 source become worse by only 30% as shown in Fig. 9 and 10.

In February 2000, during the commisioning of the HNSS hypernuclei experiment in Hall C, the chamber was put in front of the electron beam dump. There was no pile up when an approximately 1 μA, 1.8 GeV electron beam was passed directly through the chamber.

Similar techniques have been used for the measurement of the lifetime of heavy hypernuclei with the recoil shadow method and internal targets in the storage ring COSY-Julich [23]. Low pressure MWPCs have been operated at a distance of $\sim$ 30 cm from the target ($\sim 60\ \mu g/cm^2$) with $\sim 10^{10}$ protons at COSY and a cycle time of 10s. This internal target geometry corresponds to an external target experiment with an extracted beam of $\sim 1.6\mu A$ of 1.9 GeV protons.

The low-pressure technique has also been utilized to measure absolute electrofission and photofission cross sections [24][25]. In this case, the detectors were operated at a distance of $\sim$ 20 cm from the targets ($\sim 500\mu g/cm^2$) at peak electron currents of $\sim$ 10 mA (average currents were $\sim 0.5\mu A$)[25] or when a bremsstrahlung photon beam with intensity $10^9 - 10^{10}$

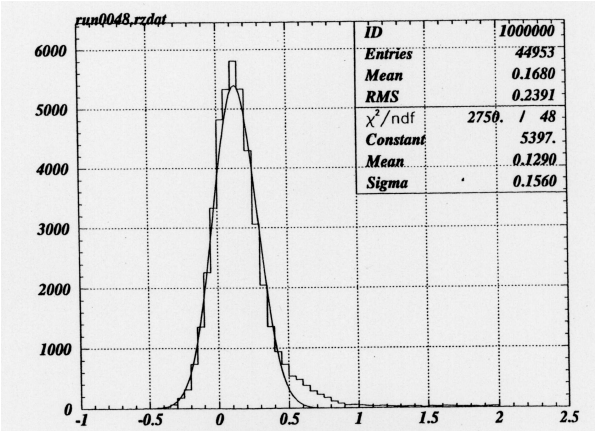

Figure 9: The time resolution of the fission fragments from a CF-252 source without beam.

photon/sec passed directly through the detector with 30 mg/cm^2 Al plus 1.0 mg/cm^2 U target inside [25].

A large area detection system which consists of twelve LPMWPCs was used in the search for exotic super-massive nuclei [26]. Stable detector operation was reached even at the highest beam intensities, with electron currents in the detectors of at most 5 μA.

Coherent π^o electroproduction on ^4He was studied using the internal target facility of the AmPS electron storage ring at NIKHEF [27][28]. The experiment was performed at a luminosity of about $10^{33} cm^{-2}/s$ with a stored beam of about 200 mA (615 MeV and 676 MeV) electrons and a ^4He and ^2H gas target of 10^{15} atoms/cm^2. The neutral pions were detected by the coincidence of the scattered electrons with the recoiling ^4He nuclei measured by a dedicated recoil detector based on the low pressure technique [28]. This detector was designed to detect light ($A \leq 4$), low-energy (0.5–24 MeV for proton and 1–95 MeV for ^4He) nuclei.

As such, we conclude that the recoil detectors based on low-pressure MWPCs can be operated at a luminosity of up to 10^{33} cm^{-2}/s.

c.) **Recoil detector based on LPMWPCs**

The gas-filled magnetic spectrometer separator has been widely exploited in experimental nuclear physics [29]-[31]. This technique is suitable for the detection and identification of low-energy recoils. We suggest to use low-pressure heptane and hexane as a gas environment in the magnetic spectrometer-separator and as a working gas for the LPMWPCs or LPMSCs simultaneously. By means of the low-pressure technique, the time-of-flight and position parameters of the low energy recoils can be determined to within a few hundred picoseconds and a few hundred micrometer precision, and consequently one can determine their velocities and magnetic rigidities within a precision of a few percent. In addition, the dE/dx of low

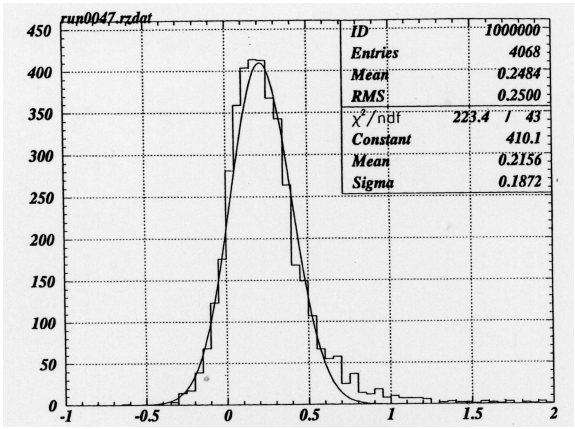

Figure 10: The time resolution of the fission fragments from a CF-252 source with beam.

energy recoils can be measured. The resolving power of the gas-filled separator can be written as:

$$(A/\delta A)_{fwhm} = 100/(\delta(BR)/BR)_{fwhm}, \tag{21}$$

where A is the ion mass, BR is the magnetic rigidity in units of Tesla-meter, and $\delta(BR)/BR)_{fwhm}$ is in %. For a 2% total BR resolution,

$$(A/\delta A)_{fwhm} = 50; (Z/\delta Z)_{fwhm} = 30. \tag{22}$$

Z is the atomic number of the ion. Such a device will have wide application in intense electron beam experiments, providing the detection and identification of low-energy recoil nuclei in a wide range of mass and charges.

In the Primakoff process with a beam energy $\sim$ 11 GeV, the recoil kinetic energy is very low ($T_{min} \sim 0.5$ MeV). The deposited energy of the recoil particles in the detector is comparable to the energy of recoils:

$$(dE/dx) \times \delta x \sim T \tag{23}$$

Thus the recoils can be identified by the measurement of the velocities V_1 and V_2, before and after the energy deposition:

$$A \times V_2^2/2 = A \times V_1^2/2 - (dE/dx) \times \delta x \tag{24}$$

and

$$A = \frac{2 \times (dE/dx) \times \delta x}{V_1^2 - V_2^2} \tag{25}$$

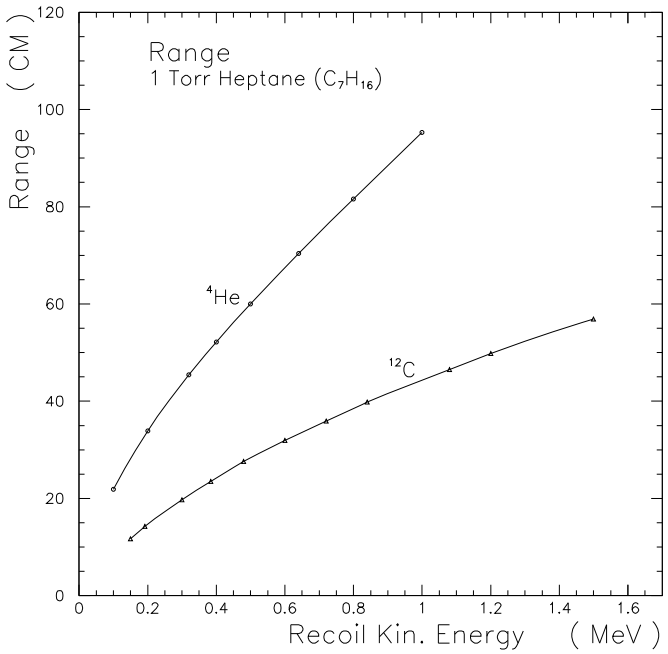

Figure 11: Range of ^4He and ^{12}C in heptane for different kinetic energy.

Figure 11 shows the range of the recoil ^4He and ^{12}C in a 1 Torr pressure Heptane gas for different kinetic energy. At ~ 0.2 MeV kinetic energies, the range of ^4He is ~ 35 cm and ^{12}C is ~ 15 cm, which indicates that the recoil nuclei in such an energy range can travel enough distance to reach the detector.

We have a preliminary conceptual design of the recoil solenoid detector. It may consist of the following three elements: (1), a solenoid magnet; (2) the 3–5 internal layers of Low Pressure Multiwire Proportional Chambers (LPMWPCs) to detect the very low energy of the recoiling nuclei; (3), a solid state detector in the outer layers (silicon strip detector or segmented scintillator detector) for the higher energy recoil particles. The detector will cover the energy range ~ 0.1–50 MeV for ^4He. Further research on this recoil detector is planned.

3.3.3 The Hybrid Calorimeter (HYCAL)

The electromagnetic decay particles from η and η', and scattered electrons in the transition form factor measurement will be detected in a highly segmented array of the Hybrid Shower Calorimeter (HYCAL) located downstream of the target. Currently our collaboration (PrimEx) is constructing a Hybrid Shower Calorimeter for an approved π^0 life time

experiment in Hall B, as shown in figure 12. We propose to use a somewhat larger version of this detector for the η and η' experiments. It will be about 150.0 x 150.0 cm^2 in the dimension transverse to the beam. The calorimeter is designed to measure both the position and the energy of electromagnetic showers using a two dimensional matrix of radiators (lead glass and crystals). That will be accomplished by choosing the cross section of the individual counters small enough so that the energy leakage into adjacent counters can be used to determine the position of the shower axis. The calorimeter will consist of two types of detectors. The outer part of the calorimeter will be made from lead glass Cherenkov detectors with the size of the radiators 4x4x40 cm^3.The excellent optical transparency and optimized transverse size of the lead glass radiator provide good energy and position resolutions:

$$\frac{\sigma_E}{E}(\%) = \frac{4.0}{\sqrt{E}} + 2.5, \sigma_x = \frac{5mm}{\sqrt{E}}, \tag{26}$$

where E is in GeV. As the Primakoff cross section peaks at extremely small angles: $\theta_\eta = 0.1^o$ at $E_\gamma = 10GeV$, in order to identify and extract the Primakoff amplitude (at very small recoil energy range, the formation of η will be determined by $\eta \to \gamma\gamma$ detection), the experimental setup must have sufficient resolution for the η production angle. This resolution depends strongly on the decay photon energy and position accuracy of the calorimeter. Therefore, the central region of the HYCAL will be constructed from lead tungstate ($PbWO_4$) crystals of size $2\times2\times20cm^3$. According to a recent report from the Mainz group, the energy resolution of similar crystals operated at a stabilized temperature (8°C) is:

$$\frac{\sigma_E}{E}(\%) = \frac{1.54}{\sqrt{E}} + 0.3, \tag{27}$$

where E is given in GeV[32]. These high resolution detectors will cover a $\sim 50 \times 50$ cm^2 area around the beam where at least one photon from the $\eta \to \gamma\gamma$ decay will hit the central part of the calorimeter. In addition, this crystal insertion will significantly improve the radiation hardness of the detector near the beam line where radiation doses can be high. The central $12 \times 12cm^2$ hole will be left open to enable the photon beam to pass through. The modules contiguous with this region on the beam axis as well as the two outermost layers of modules in the lead glass wall will be excluded from the fiducial volume of the detector to control coordinate resolution and detection efficiency near the boundaries of the detector. To monitor and correct possible gain changes due to temperature and aging, a light monitoring system will be used. Details of the detector design can be found in the Conceptual Design Report of the π^0 life time measurement experiment.

3.3.4 Background Veto Detector

The main source of background in the recoil detector arises from the recoiling nuclei from elastic electron scattering in the target, and the main background in the hybrid calorimeter is the Møller electrons. Offline, we will be able to distinguish the recoil events from η and η' production, which are of interest, from the elastic background. This is because their

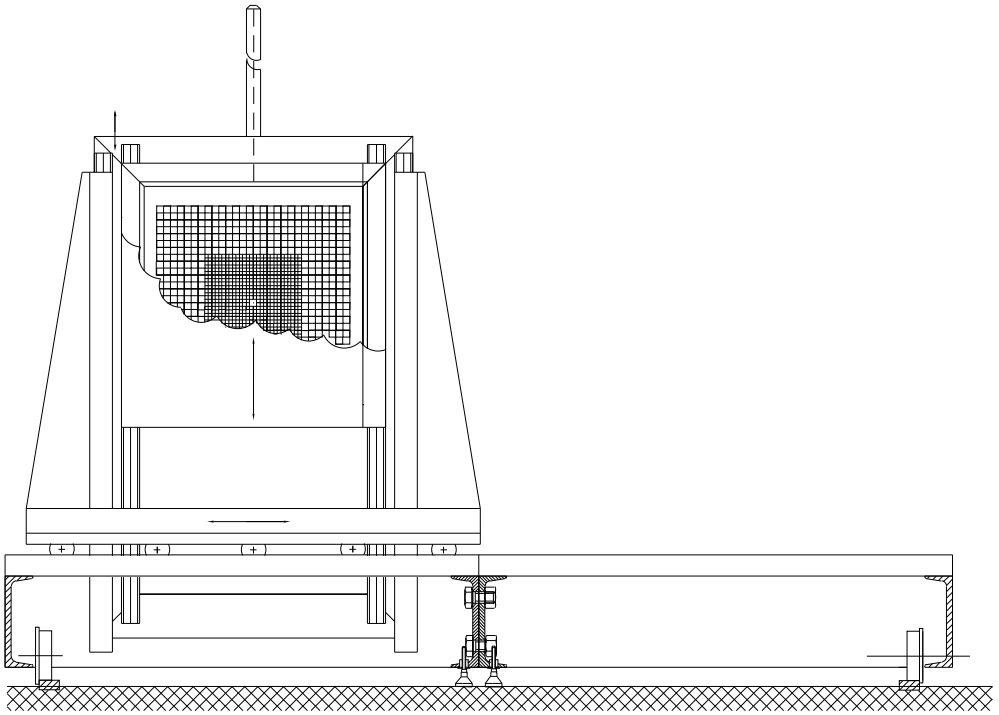

Figure 12: Schematic view of the HYCAL electromagnetic calorimeter with the transporter.

kinematics are very different. As shown in figure 13 and 14, the elastic recoil angle is located near 90^0, while the meson's production angle is smaller. The Primakoff cross section is peaked at a recoil angle of around 40°. On the other hand, the Møller events are also kinematically different from the η and η' decay events in the calorimeter. The Møller events consist of two charged electrons with total energy equaling that of the beam energy, while the η and η' decay events are usually accompanied by at least one γ. This allows one to separate them offline. Online, we will use a background veto detector to cut down both elastic and Møller background at the trigger level. (see figure 15). In addition, the prescaled elastic events can also be used to calibrate the recoil detector and monitor the luminosity.

We estimate the rates by assuming a 1μA electron beam ($N_e \sim 6.26 \times 10^{12}$ electron/sec), impinging upon a 40 cm heptane (C_7H_{16}) gas target at 1 torr, which corresponds to $N_{^{12}C} \sim 10^{19}\ atoms/cm^2$. The elastic scattering cross section is:

$$\sigma_{el} = \int_{0.02MeV}^{\infty} \frac{d\sigma}{dT}(e,^{12}C)dT \sim 6.0mbarn \tag{28}$$

Therefore, the total elastic background rate from ^{12}C is:

$$\begin{aligned} N_{elastic} &= N_e \cdot N_{^{12}C} \cdot \sigma_{el} && (29)\\ &= 6.25 \times 10^{12} \times 10^{19} \times 6 \times 10^{-27} && (30)\\ &\sim 4. \times 10^5 Hz && (31) \end{aligned}$$

On the other hand, for a $150cm \times 150cm$ hybrid calorimeter with $12cm \times 12cm$ central hole to allow the beam to pass through, located ~ 5 meters downstream from the target, the Møller electron background rate on the calorimeter is ~ 67 kHz. In order to veto both elastic and Møller background at the trigger level, we will build a background veto detector, located ~ 20 meters downstream of the target. It will be about $50 \times 50\ cm^2$ in the dimension

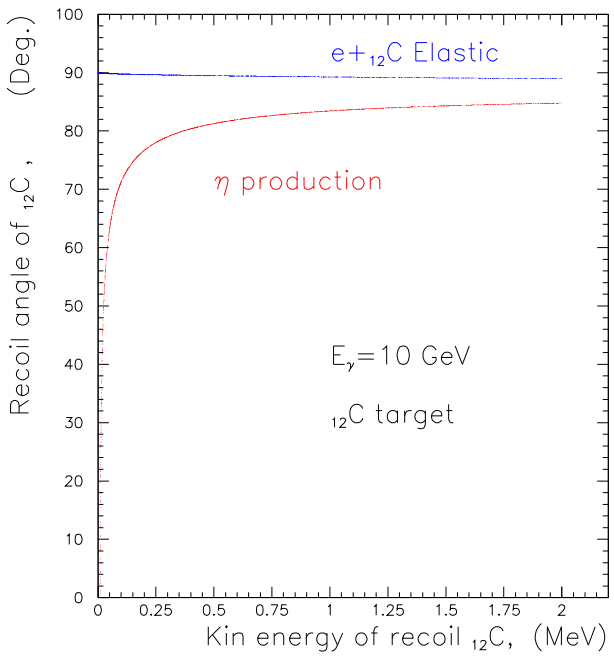

Figure 13: Kinematics of recoil ^{12}C from the η production reaction and elastic scattering.

transverse to the beam, with a $4 \times 4cm^2$ hole in the middle. The detector will be constructed from lead tungstate ($PbWO_4$) crystals of size $2 \times 2 \times 20cm^3$.

Figure 16 shows the Monte Carlo result from a total of 22,000 elastic (e,^{12}C) events. In the figure, (a) shows the elastic electron hit distribution on the hybrid calorimeter without any cut with 44 out of 22000 total events, which means the elastic background will have a very small effect on the calorimeter because of the small electron scattering angle; Figure (c) shows the elastic electrons hitting the background veto monitor detector, with 19956 out of 22000 events; Figure (b) shows the kinetic energy spectrum of recoiling ^{12}C nuclei from elastic scattering before the veto monitor cut, which indicates that the recoil background from the elastic scattering is mostly at small recoil energy. Figure (d) shows the kinetic energy spectrum of the recoiling ^{12}C nuclei from elastic scattering after the veto monitor cut, with only 44 out of 22000 events left. Therefore, the elastic background in the recoil detector is reduced 2×10^{-3} times by the veto monitor. For a 1μA electron beam, we will have a $4 \times 10^5 \times 2 \times 10^{-3} \sim 800Hz/\mu A$ elastic background left in the recoil detector and the calorimeter after the cut, and the elastic rate on the veto monitor is about 400 KHz per μA electron beam current.

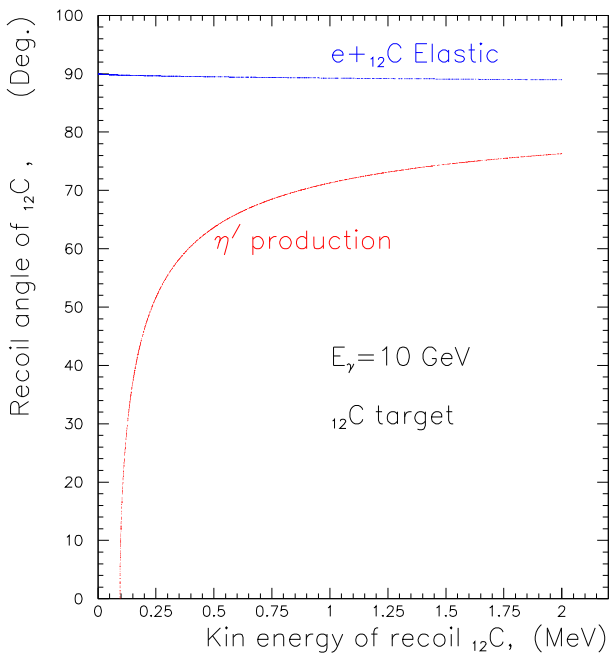

Figure 14: Kinematics of recoil ^{12}C from η' production reaction and elastics scattering.

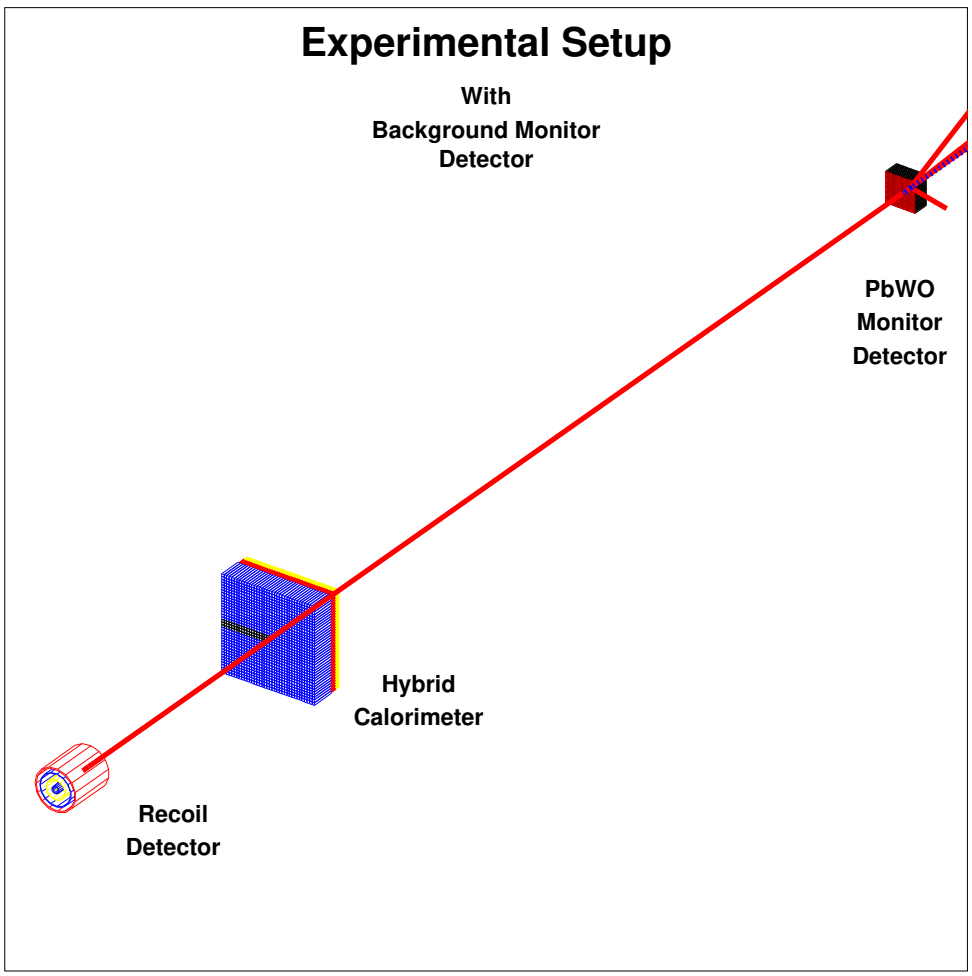

Figure 15: Background veto detector setup.

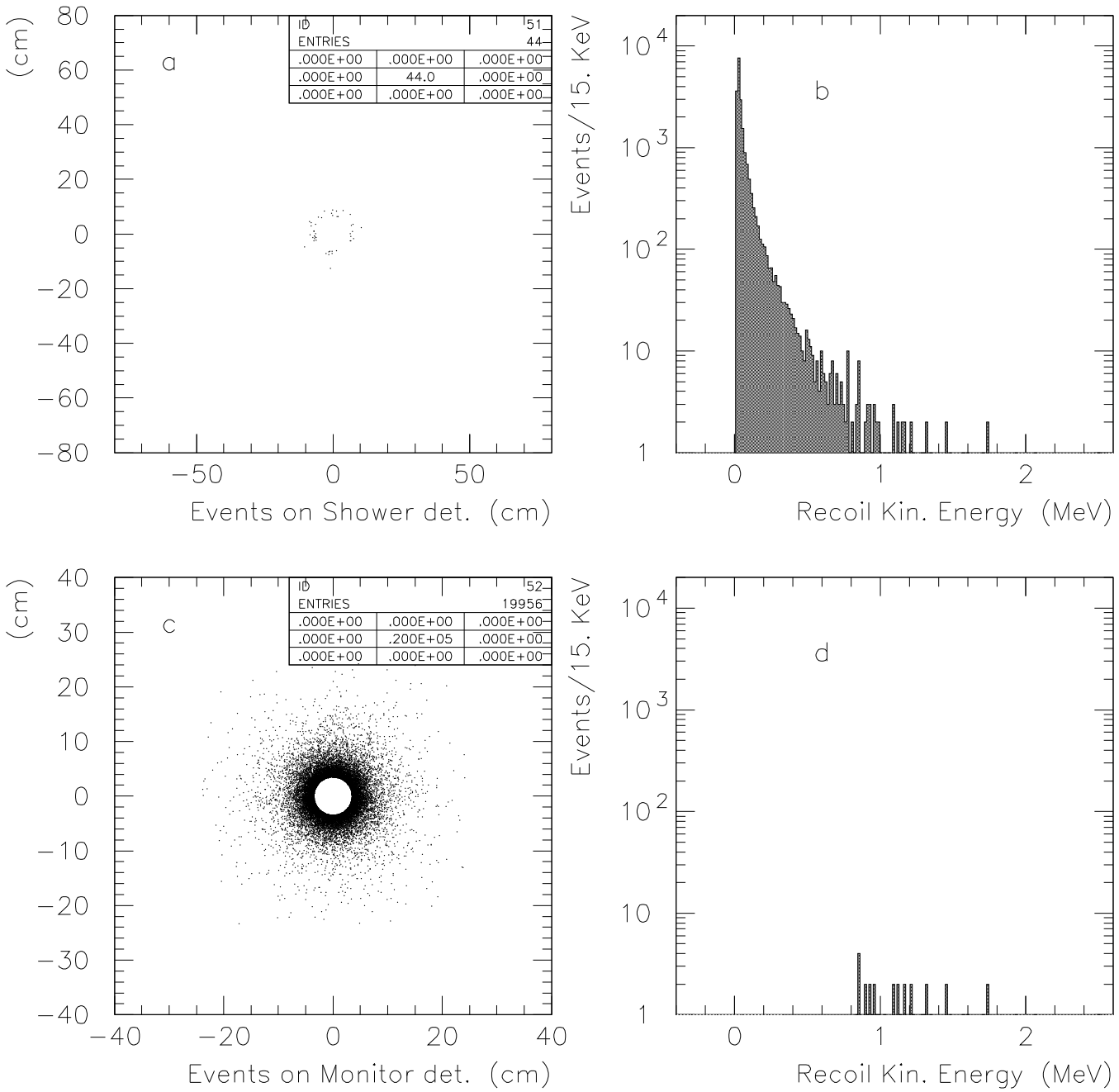

Figure 16: Monte Carlo simulation for $(e,^{12}C)$ elastic background

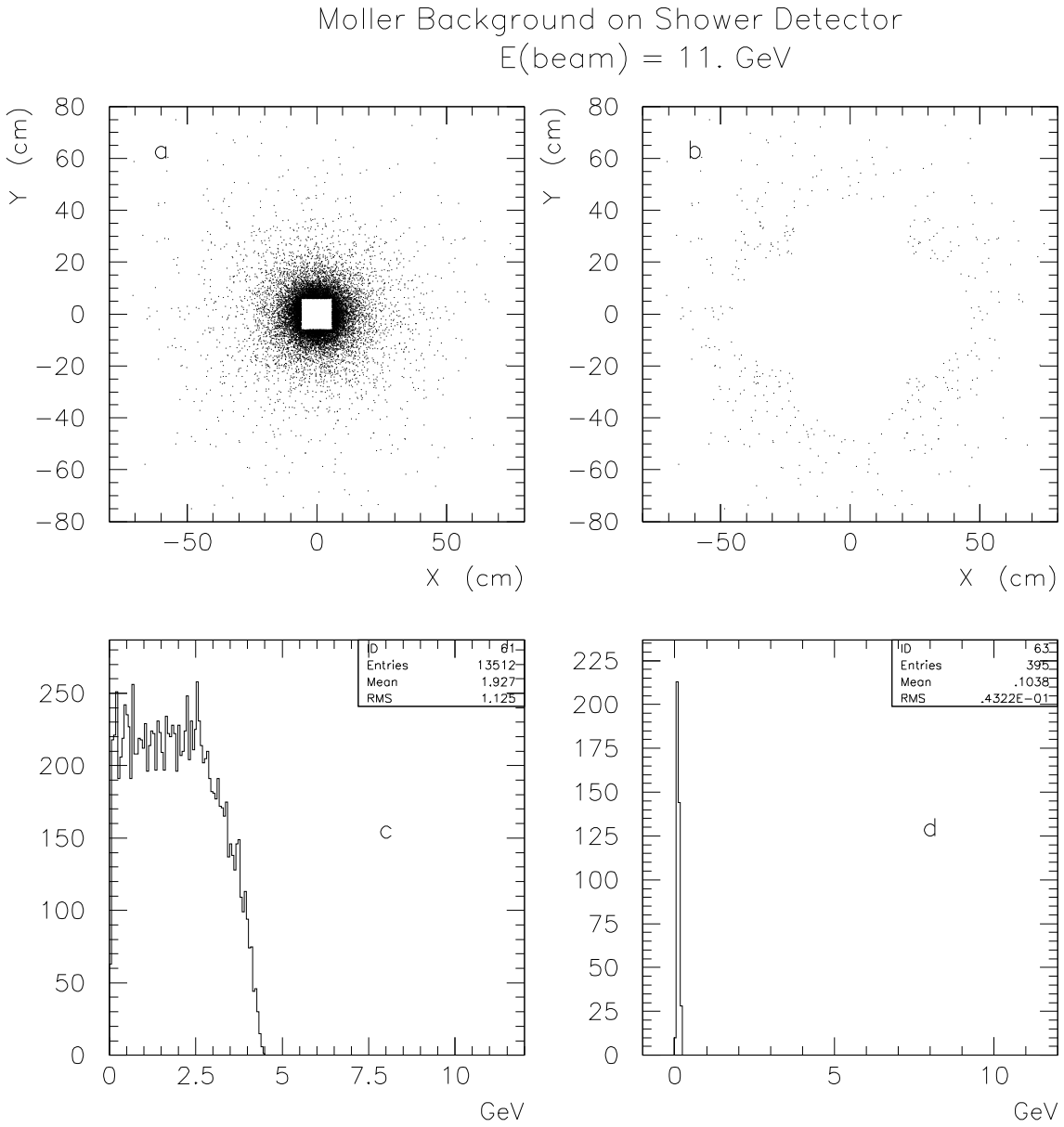

Figure 17: Monte Carlo simulation for Møller background on the shower detector.

Figure 17 shows the Monte Carlo result simulated from a total of 20,000 Møller events. In the figure, (a) and (c) show the position distribution and energy spectrum of Møller electrons hitting the hybrid calorimeter before the veto monitor cut, and the total hits on the detector is 13512; (b) and (d) show the position distribution and energy spectrum of Møller electrons on the hybrid calorimeter after the veto monitor detector cut, about 395 events left compared with before the cut, and (d) also indicates that only very small energy Møller events can survive from the veto detector cut, which can be cut eventually by setting detector energy threshold to about 1 GeV.

According to the cross section, the Møller event rate is about 10^5 Hz per 1μA electron

beam. Thus, without a veto monitor cut, the Møller event rate on the calorimeter will be:

$$N_m \sim 1. \times 10^5 \times \frac{13500}{20 \times 10^3} \quad (32)$$

$$\sim 67.5 \times 10^3 electron/sec. \quad (33)$$

When adding the veto monitor cut, the Møller event rate will be reduced to:

$$N'_m \sim 1. \times 10^5 \times \frac{400}{20 \times 10^3} \quad (34)$$

$$\sim 2 \times 10^3 electron/sec \quad (35)$$

The Møller event rate on veto monitor detector is $\sim 2 \times 10^5$ electron/sec.

In summary, implementing the background veto monitor detector will greatly help to reduce both elastic and Møller background in the recoil detector and the hybrid calorimeter.

3.4 Rates and Uncertainties

One can ensure a clean separation of the Primakoff mechanism from background photoproduction processes by exploiting the known Primakoff cross section's energy, Z^2, and angular dependence. As such, we propose measurements on different nuclei (^4He and ^{12}C discussed here), a range of energies, and over a range of angles as determined by the hybrid calorimeter (HYCAL).

Figure 18 shows a Monte Carlo simulation of the expected experimentally measured angular distribution of $\eta \to \gamma\gamma$ events on ^4He, where the resolution and geometrical acceptance of the hybrid calorimeter were taken into account. The target thickness was taken to be 2×10^{19} helium atoms/cm^2 and the calorimeter is $1.5m \times 1.5m$ and is 5 meters downstream of the target. Because the $\eta \to \gamma\gamma$ branching ratio is well known, the η is reconstructed by measuring 2γ in the calorimeter. The simulation corresponds to 30 days of beamtime at $5\mu Amps$, and yields 20,500 $\gamma\gamma$ events. A fit to these data results in a $\Gamma^{\eta}_{\gamma\gamma} = 0.4603$keV with a 1.8% statistical error. In comparison, the data were generated using the value from the Particle Data Book of 0.463 keV.

A Monte Carlo simulation of η production on ^{12}C was also performed (see figure 19) assuming a target thickness of 2×10^{19} carbon atoms/cm^2. As with the previous simulation, the calculation corresponds to $5\mu Amps$ of beam current for 30 days. It is worth noting, however, that with the proposed setup involving recoil detection with low pressure multiwire proportional counters, where the chamber working gas heptane will be used as a target, the helium and carbon data would be obtained simultaneously. The simulation yields 72,500 $\eta \to \gamma\gamma$ events and gives a 0.7% statistical error on the width. The estimated experimental uncertainties for $\Gamma(\eta \to \gamma\gamma)$ is listed in the table 1.

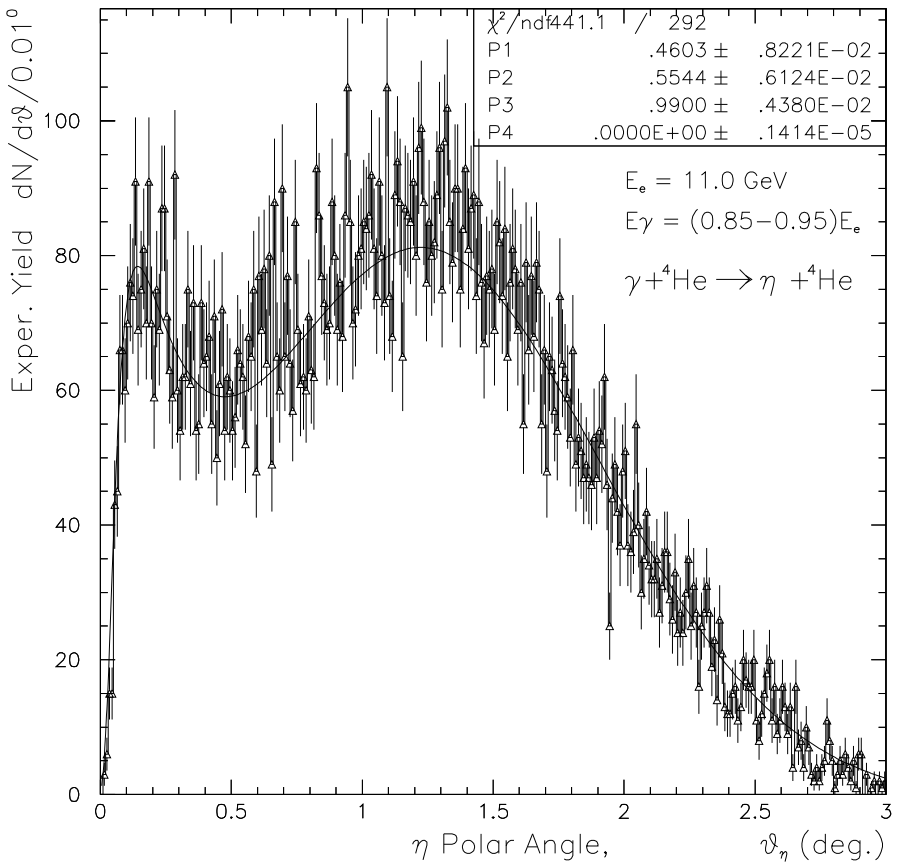

Figure 18: Monte Carlo simulation of experimentally measured angular distribution of $\eta\gamma\gamma$ events on ^4He.

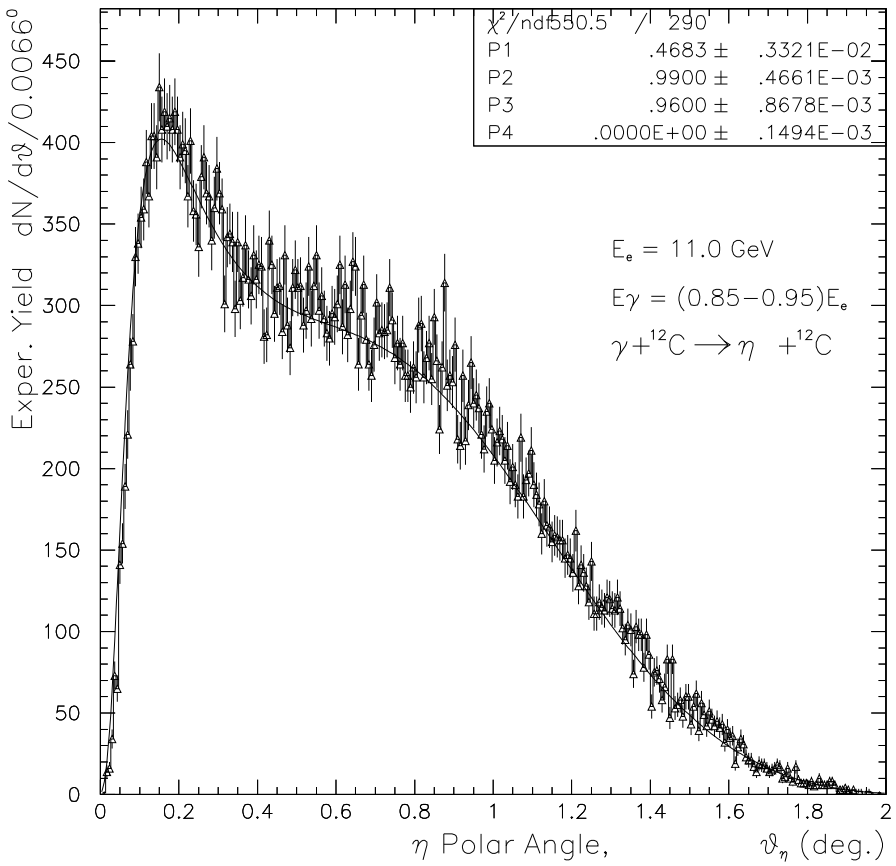

Figure 19: Monte Carlo simulation of experimentally measured angular distribution of $\eta\gamma\gamma$ events on ^{12}C.

Statistical	$< 1.\%$ (30 days)
photon flux	1.%
target thickness	1.%
acceptance, misalignment	0.4%
background subtract	0.3%
beam energy	0.2%
distorted form factor	0.3%
branching ratio	0.8% (PDB)
Total	2.0%

Table 1: Estimation of the experimental uncertainties for $\Gamma(\eta \to \gamma\gamma)$ measurement.

Because of the poor knowledge of the η' decay branching ratios, we will directly use the missing mass reconstructed by recoil detection to identify the η'. One γ registered in the calorimeter will be required in the trigger to cut off the background, such as ρ photoproduction. Figure 20 shows the simulated missing mass spectrum with all physical backgrounds except multi-pion production. The η' production rate will be similar to that of η. The estimated total error for the η' width is $\sim$ 3–4%.

3.5 Improvement on the η–η' Mixing Angle

As discussed earlier, the η–η' mixing angle is determined by:

$$\begin{aligned}
\Gamma(\eta \to \gamma\gamma) &= \frac{\alpha_{\rm em}^2}{64\pi^3}\frac{M_\eta^3}{3f_\pi^2}\left[\frac{f_\pi}{\bar{f}_{\eta 8}}\cos\theta - \sqrt{8}\frac{f_\pi}{\bar{f}_{\eta 0}}\sin\theta\right]^2 , \\
\Gamma(\eta' \to \gamma\gamma) &= \frac{\alpha_{\rm em}^2}{64\pi^3}\frac{M_{\eta'}^3}{3f_\pi^2}\left[\frac{f_\pi}{\bar{f}_{\eta 8}}\sin\theta + \sqrt{8}\frac{f_\pi}{\bar{f}_{\eta 0}}\cos\theta\right]^2 .
\end{aligned} \tag{36}$$

If one calculates the $\frac{f_\pi}{\bar{f}_{\eta 8}}$ by using the leading log prediction of one-loop chiral perturbation theory[5]:

$$\frac{f_\pi}{\bar{f}_{\eta 8}} = 1 - \frac{m_k^2}{(4\pi f_\pi)^2}\ln\frac{m_k^2}{(4\pi f_\pi)^2} + \frac{m_\pi^2}{(4\pi f_\pi)^2} \tag{37}$$

where the experimental value of the pion decay constant is $f_\pi = 92.42 \pm 0.25$ MeV. Then $\frac{f_\pi}{\bar{f}_{\eta 0}}$ can be determined independent of the mixing angle from the π^0, η and η' two-gamma decay widths:

$$R \equiv \left[\frac{\Gamma(\eta \to \gamma\gamma)}{M_\eta^3} + \frac{\Gamma(\eta' \to \gamma\gamma)}{M_{\eta'}^3}\right]\frac{M_\pi^3}{\Gamma(\pi^0 \to \gamma\gamma)} = \frac{1}{3}\left(\frac{f_\pi^2}{\bar{f}_{\eta 8}^2} + 8\,\frac{f_\pi^2}{\bar{f}_{\eta 0}^2}\right) , \tag{38}$$

Therefore, the mixing angle can be calculated from equation 36.

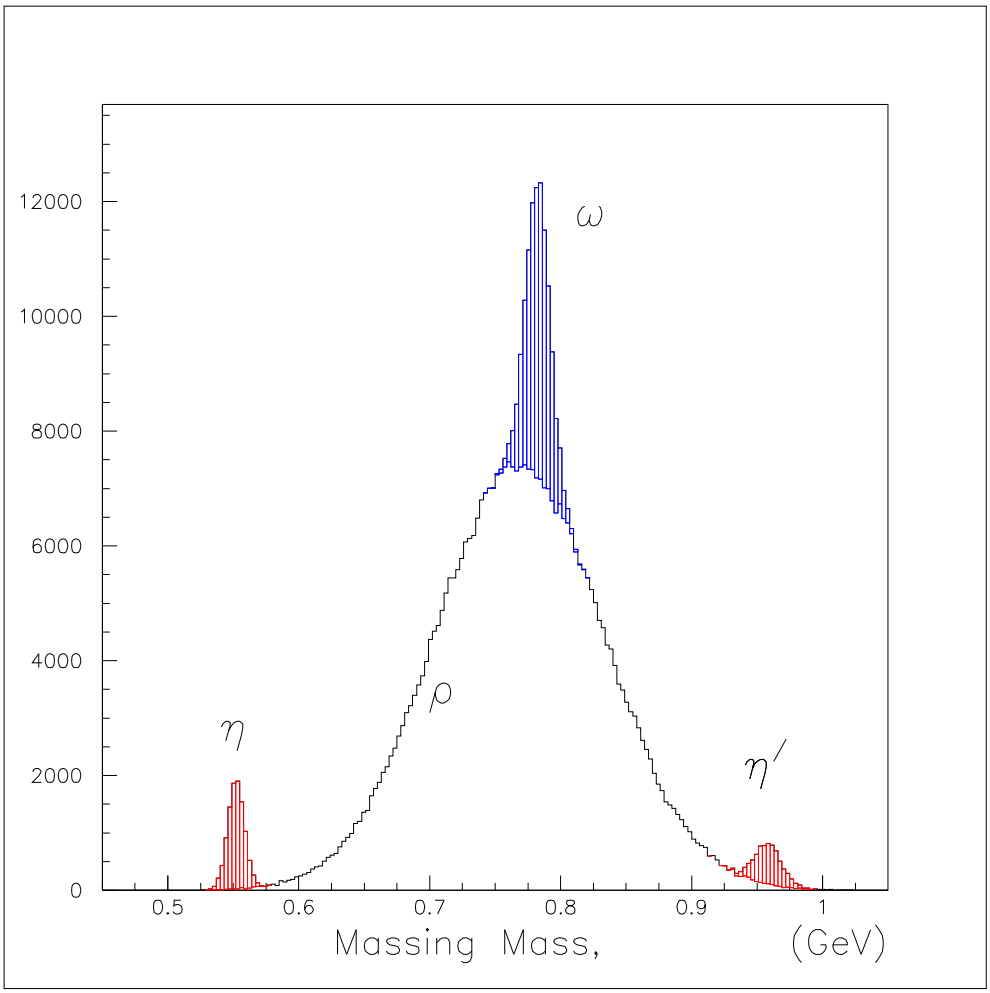

Figure 20: Monte Carlo simulation of the missing mass spectrum for ^4He target, with physical backgrounds except multi-pion production.

If one uses the current average values of the π^0, η and η' two-gamma decay widths listed in the Particle Data Book: $\Gamma(\pi^0 \to \gamma\gamma) = 7.74 \pm 0.55$eV, $\Gamma(\eta \to \gamma\gamma) = 0.46 \pm 0.04$keV, and $\Gamma(\eta' \to \gamma\gamma) = 4.37 \pm 0.25$keV, the mixing angle and $\bar{f}_{\eta_0}$ will be:

$$\begin{aligned} \theta &= -20.75^o \pm 1.64^o \\ \bar{f}_{\eta_0} &= 1.08 \pm 0.05 f_\pi \end{aligned} \tag{39}$$

which indicates about an 8% error on the mixing angle and a 4.6% error on $\bar{f}_{\eta_0}$. On the other hand, if applying the 1.5% error on $\Gamma(\pi^0 \to \gamma\gamma)$ as proposed in the approved π^0 life time measurement experiment ($\Gamma(\pi^0 \to \gamma\gamma) = 7.74 \pm 0.11$eV), and 2% error on $\Gamma(\eta \to \gamma\gamma)$ as proposed in this experiment ($\Gamma(\eta \to \gamma\gamma) = 0.46 \pm 9.2 \times 10^{-3}$keV), while keeping the error on $\Gamma(\eta' \to \gamma\gamma)$ still the same as Particle Data Book average, with the central values of each width arbitrarily chosen to agree with the Particle Data Book average, one will get:

$$\begin{aligned} \theta &= -20.75^o \pm 0.61^o \\ \bar{f}_{\eta_0} &= 1.08 \pm 0.02 f_\pi \end{aligned} \tag{40}$$

It shows that the error on η–η' mixing angle reduces to $\sim 3\%$ and the error on $\bar{f}_{\eta_0}$ becomes $\sim 2\%$.

Furthermore, if using the error on the two-gamma decay widths of all three particles π^0,η and η' as suggested by this program: $\Gamma(\pi^0 \to \gamma\gamma) = 7.74 \pm 0.11$eV, $\Gamma(\eta \to \gamma\gamma) = 0.46 \pm 9.2 \times 10^{-3}$keV, and $\Gamma(\eta' \to \gamma\gamma) = 4.37 \pm 0.13$keV, the result would become:

$$\begin{aligned} \theta &= -20.75^o \pm 0.44^o \\ \bar{f}_{\eta_0} &= 1.08 \pm 0.01 f_\pi \end{aligned} \tag{41}$$

The η–η' mixing angle error would further reduce to $\sim 2\%$ and the error on $\bar{f}_{\eta_0}$ would become 1.4%. As one can see, the proposed experimental program will significantly improve our understanding on both the η–η' mixing angle and the decay constant $\bar{f}_{\eta_0}$.

4 Measurements of the Transition Form Factors $F_{\gamma\gamma^* P}$

Studies of the $\gamma\gamma^* P$ vertex, where P represents the π^o, η, or η' pseudoscalar mesons and γ^* is a virtual photon of low or moderate Q^2, enable one to study the transition regime from soft nonperturbative physics to the hard processes of perturbative QCD. We propose to measure the photon momentum dependence of the form factors $F_{\gamma\gamma^* P}(Q^2)$ and thereby map out an extension to the axial anomaly to provide a clean test of QCD predictions for exclusive processes.

The structure of the meson's electromagnetic coupling is typically parameterized in the context of the vector meson dominance model in which a photon couples to hadronic matter via an intermediate vector meson. Such a model implies a form factor of the form:

$$F_\pi = \frac{1}{1 + q_\mu^2 / m_V}, \tag{42}$$

where m_V is the mass of the vector meson. For the charged pion case, the Coulomb form factor has been measured[33] and the charge radius was determined to be about 0.6 fm. Due to charge conjugation symmetry, however, the elastic Coulomb form factor (γPP) vanishes. The $\gamma^*\gamma P$ transition vertex, on the other hand, is of great interest and has been studied theoretically from the point of view of models based on the VDM as well as those involving treatments of the quark substructure[34]. This transition is characterized by the form factor $F(q_1^2, q_2^2)$ which, if only one photon is significantly off shell, depends upon a form factor typically parameterized by the pole form (9), and approximated at low q_μ^2 by:

$$F_{\gamma^*\gamma\pi^o} \approx 1 - a\frac{q_\mu^2}{m_P^2}. \tag{43}$$

where a is a measure of the $\gamma^*\gamma P$ interaction radius.

The low, as well as high, Q^2 behavior of this form factor has been the source of considerable theoretical efforts. As pointed out in Bijnens [48], the next to leading order contributions are quite different when one of the photons is off shell. While the loop contributions tend to cancel when both photons are real, they have significant effect in the virtual case.

Recently, Maris and Tandy [46] have used the ladder Bethe-Saltpeter solution for the dressed photon-quark vertex to study the low momentum behavior using model parameters fixed by the light meson masses and decay constants. They show that the often-used Ball-Chiu ansatz for the vertex is deficient. The results of their calculation are shown in figure 21, where the dot-dash line uses the bare vertex, the dashed is the Ball-Chiu ansatz, and the solid line is their calculation.

Frank [47], have calculated $F_{\gamma^*\gamma\pi^o}$ from a generalized impulse approximation within a QCD-based model field theory which gives a good description of the charged pion form factor. Their approach uses dressed vertices and propagators consistent with dynamical chiral symmetry breaking, gauge invariance, quark confinement, and perturbative QCD. Their results are shown in figure 22, where they find a $\pi\gamma\gamma$ interaction radius of $0.47fm$.

Ivanov and Lyubovitskij calculate the form factor within a Lagrangian quark model with a separable interaction known to provide a good description of the pion observables at low energies. With their gaussian pion-quark vertex, they obtain an $r_{\pi^o} = 0.65fm$. Their results are indicated by the dashed line in the figure 23.

Despite the theoretical interest in pseudscalar meson form factors, the experimental situation remains incomplete. Here, we indicate the experiments which have been performed, and the contributions which could be made with 11 GeV electron beams using the virtual Primakoff effect.

4.1 Previous Measurements in the Space-like Region

A number of experiments have been performed to measure these transition form factors. While great progress has been made in the high Q^2 region, data at low and intermediate regime are currently quite poor. The CELLO collaboration at PETRA has measured $F_{\gamma^*\gamma P}$ in the space-like region at large momentum transfers using the reaction $e^+e^- \rightarrow e^+e^-P$[7].

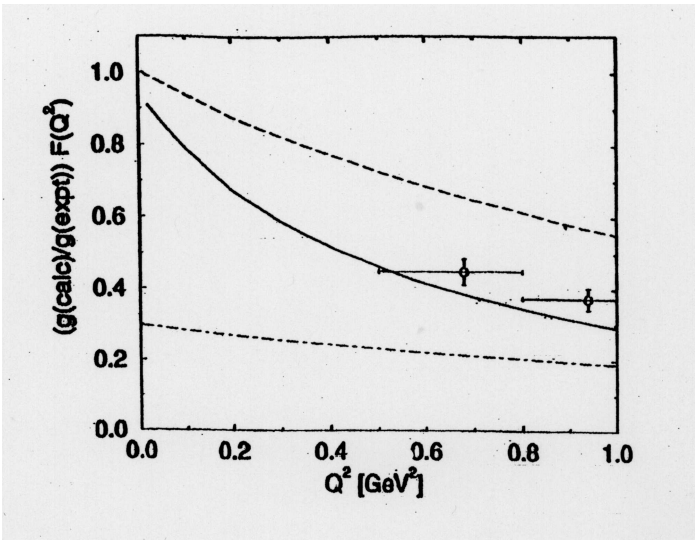

Figure 21: The $\gamma^*\gamma\pi^o$ transition form factor using a bare vertex (dot-dash), and the BC Ansatz (dashed) and the numerical solution of Maris and Tandy.

In this experiment two photons are radiated virtually by the colliding e^+e^- beams. One of the virtual photons is close to real and the other has a larger q_μ^2 and is tagged by the detection of an e^+ or e^-.

Measurements were taken at momentum transfers ranging from 0.62 to 2.17 $(GeV/c)^2$, and the value of a was deduced by extrapolation under the assumption of vector meson dominance. For the pion, the authors quote a value of $a = 0.0325 \pm 0.0026$ (statistical) with systematic errors estimated to be of the same order as the statistical error. The results of these measurements are shown in figure 24 with the corresponding fit to $F_{\gamma^*\gamma P}$. From the plot, it is clear that any extraction of the slope parameter at $Q^2 = 0$ is highly model dependent. Data covering the higher q_μ^2 region from 2 to 20 GeV^2 have also been reported by the CLEO collaboration[49]. High Q^2 measurements on the η and η' have been performed

as well.

A conditionally approved experiment in Hall A (E97-009) will measure this form factor in the very low q_μ^2 regime ranging from 0.005 to about 0.035 $(GeV/c)^2$ to extract a. This leaves the intermediate momentum transfer region for the pion largely unexplored experimentally. While the L3 Collaboration has some results (with very poor Q^2 resolution) in the low Q^2 region for the η', low and intermediate Q^2 data on the η are totally lacking. The advent of 11 GeV electrons at TJNAF, however, will make such studies possible.

4.2 Previous Experiments in the Time-like Region

A number of experiments aimed at measuring a have been performed in the time-like momentum transfer region utilizing the π^o and η Dalitz decay $\pi^o/\eta \rightarrow e^+e^-\gamma$ reaction [35][36][37][38][39][40] [41][42][43][44], as shown in figure 25. The amplitude for this process involves the $F_{\gamma^*\gamma P}$ form factor which, in the usual linear expansion

$$F(x) \approx 1 + a\frac{m_{e^+e^-}^2}{m_P^2}. \tag{44}$$

A summary of these measurements on the pion is shown in the figure 25, where it can be seen that the published values for the slope range from -0.24 to $+0.12$. Such experiments suffer from small kinematically accessible ranges and significant backgrounds, and they require large final-state radiative corrections. As such, these experiments have not been able to determine even the sign of the form factor slope.

4.3 The Proposed Experiment

In 1989, Hadjimichael and Fallieros[45] suggested that the virtual Primakoff effect could access additional fundamental information about the pion as the cross section is proportional to $|F_{\gamma^*\gamma\pi^o}(q_\mu^2)|^2$. The full expression for the virtual Primakoff scattering cross section is[45]:

$$\begin{aligned}\frac{d^3\sigma}{d\epsilon_2 d\Omega_2 d\Omega_\pi} &= \frac{Z^2\eta^2}{\pi}\sigma_M\frac{Q^4}{K^4}\frac{\beta_\pi^{-1}}{\omega_\pi}|F_N(K^2)|^2|F_{\gamma^*\gamma\pi^o}(q_\mu^2)|^2 sin^2(\frac{\theta_e}{2})sin^2(\theta_\pi) \\ &\quad \times[4\epsilon_1\epsilon_2 sin^2\phi_\pi + |\vec{q}|^2/cos^2(\frac{\theta_e}{2})]\end{aligned} \tag{45}$$

where σ_M is the Mott cross section, $\eta^2 = (4/\pi m^3)/\tau$, τ is the π^o lifetime, K is the (nearly real) photon four momentum from the Coulomb field, the pion four momentum is $Q = (\vec{q}, \omega_\pi)$, $\beta_\pi = \vec{q}/\omega_\pi$, and $F_N(K^2)$ is the nuclear form factor. This expression for the cross section in similar to that for the real Primakoff effect, with the notable exception of the form factor $|F_{\gamma^*\gamma\pi^o}(q_\mu^2)|^2$ which is of interest here.

Hadjimichael and Fallieros examined the sensitivity of the cross section to a for energy transfers up to 1.6 GeV. They saw only moderate sensitivity and noted that the cross section is optimized for $\theta_e \rightarrow 0$ and $\theta_\pi \rightarrow 0$ whereas pion energies above 2 GeV are favored for probing

the $\gamma^*\gamma\pi^o$ vertex. We have extended these calculations to kinematical regimes available with the proposed 11 GeV electron beam at TJNAF and note that good sensitivity to the $\gamma^*\gamma P$ form factor is present.

Figure 26 shows the cross sections for the virtual Primakoff pion photoproduction process on helium-4 as a function of $E_{e'}$, an electron scattering angle of 2 degrees and a pion angle of 0.1 degrees with respect to $\vec{q}$. The incident energy is 11 GeV. The two curves are for the VDM prediction ($a = 0.03$) and that using the slope parameter determined by the $\pi^o \rightarrow e^+e^-\gamma$ experiment ($a = 0.1$) of reference [40]. From the plot one can see that the cross sections are large, and are quite sensitive to the pion transition form factor. If we define a figure of merit to be the difference in the predicted cross section for the two form factors times the square root of the average cross section, figure 27, we see that the optimal kinematics are at θ_e=2 degrees and $\omega \approx 6$ GeV.

4.3.1 Experimental Setup for Transition Form Factor Measurements

We have investigated the Q^2 acceptance available for an experimental setup in which both the scattered electron and the two photons from the meson decay are detected in the previously described hybrid calorimeter (see figure 28). The calorimeter is $1.5m \times 1.5m$, is $7m$ downstream of the target, and has a $12cm \times 12cm$ central hole to allow the beam to pass through. For such a setup, the phase space for Q^2 acceptance is shown in figure 29, where the electron scattering angle and energy transfer are restricted to regions in which the figure of merit is largest (θ_e between 0.5 and 6 degrees, ν between 2 and 10 GeV). It can be seen that this setup complements the CELLO measurements in covering the extremely low Q^2 region which is unavailable to the collider experiments.

Figure 30 shows the resolution in Q^2 at $Q^2 = 0.01GeV^2$ resulting from finite position and energy resolutions in the detection of the scattered electrons in the hybrid calorimeter. It can be seen that the Q^2 resolution is more than adequate to extract the Q^2 dependence of $F_{\gamma\gamma^*P}$.

4.3.2 Rates for $F_{\gamma\gamma^*\pi^o}$ and $F_{\gamma\gamma^*\eta^o}$

Figure 31 shows the cross section as a function of θ_π for Primakoff, coherent nuclear, and interference photoproduction processes. It can be seen that clean separation is possible. The analogous curves for the η figure of merit and cross section are shown in figures 32 and 33.

With this experimental setup, we expect a yield of 3900 π^o's and 600 η's per day. This assumes a 10^{-5} radiation length ^4He target, and a $5\mu Amp$ 11 GeV electron beam. The two photon acceptance of the hybrid calorimeter was taken to be 50%, and the branching ration for two photon decay of the η was taken to be 39%.

A Monte Carlo simulation of η transition form factor on ^{12}C was performed (see figure 34) assuming a target thickness of 2×10^{19} carbon atoms/cm^2. For 30 days running period, with $5\mu Amp$ electron beam and 50% detection efficiency, the total yield is about 50500.

5 Other Two Photon Reactions: $\gamma\gamma \rightarrow \pi\pi$

Two photon processes are a very useful probe for studying the structure of matter. Earlier sections of this white paper have detailed our plans to measure the radiative widths and very low Q^2 formfactors of the pseudo-scalar mesons π^0, η, and η'. With the availability of 11 GeV beam at JLab it will also be possible to make measurements of the $\gamma\gamma \rightarrow \pi\pi$ reaction. This section outlines the theoretical and experimental issues that make measurements of this reaction a topical subject for consideration as the nuclear physics community makes plans to upgrade the energy of JLab to 11 GeV.

Existing $\gamma\gamma \rightarrow \pi^+\pi^-$ and $\gamma\gamma \rightarrow \pi^0\pi^0$ data are from the Mark II and the Crystal Ball collaborations, respectively, and are very limited in terms of coverage and statistics. The charged pion cross sections are almost nonexistent from threshold up to 550 MeV, with 5 data points clustered near 370 MeV. The neutral pion total cross sections extend down to threshold, however the energy binning is coarse, 50 MeV, and the shape of the cross section near threshold is poorly defined. The statistical precision of the data points are low, typically 20 percent. Energy binning for the neutral pion angular distributions is even coarser, 200 MeV.

There is a great deal of theoretical interest in measurements of the $\gamma\gamma \rightarrow \pi\pi$ reaction. The near threshold reaction is generally regarded as one of the important theoretical laboratories for testing ChPT. While the charged pion production data is in good agreement with ChPT, the one-loop calculation is completely inadequate to describe the neutral pion production data. Higher order processes, such as multi-loop effects, are believed to play an important role in the neutral channel, making this channel a severe challenge for theory. The most successful theoretical description of the threshold two pion data has been by Donoghue and Holstein [52]. In their calculation they matched the low-energy chiral amplitude with that given by a full dispersive treatment, obtaining good agreement with experiment. However, as previously noted, the existing experimental data do not provide an adequate test of the theory.

Two pion production is of interest for phenomenological reasons as well. The data have been used to extract the π^+ and π^0 polarizabilities [50], providing one of three complimentary means for determining the pion polarizabilities. The other methods involve Compton scattering techniques; Compton scattering from a virtual pion in the $\gamma p \rightarrow \pi^+\gamma n$ reaction, and photon production in a pion induced Primakoff reaction, i.e. $\pi\gamma \rightarrow \pi\gamma$. In the Compton scattering reactions the forward cross section is sensitive to the sum of the electric and magnetic polarizabilities, $\alpha_E + \beta_M$, and the backward cross section is sensitive to $\alpha_E - \beta_M$.

Two photon data are sensitive to $\alpha_E - \beta_M$ because the photons are colinear in the C.M. frame.

The existing data on the charged and neutral pion polarizabilities are in poor agreement with each other and with theory [52]. A new measurement of the charged pion polarizability through pion photo-production on the proton is underway at Mainz. At CERN the COMPASS collaboration has plans to measure the pion Primakoff reaction. Because of the inherent errors in these measurements, model-dependent for the analysis of pion photoproduction on the proton and statistical for the Primakoff experiment, we believe it is important to obtain measurements of the polarizabilities through other complimentary reactions. Donoghue and Holstein's calculation has shown that the existing two pion data from Mark II and Crystal Ball are inadequate to provide useful constraints on the pion polarizabilities. Data with greater accuracy over the $\pi\pi$ energy range from threshold to 500 MeV are required.

Pennington has suggested that $\gamma\gamma \rightarrow \pi\pi$ data can help solve the riddle of the σ meson [53]. The PDG name for the σ is the $f_0(400-1200)$. σ exchange plays an important role in generating the medium range attraction in the nucleon-nucleon force, and is equivalent to an I=0 S-wave two pion exchange process. It is an open question as to whether this interaction actually behaves as the exchange of a short-lived particle since the direct channel I=0 $\pi\pi$ S-wave cross sections show no evidence for a Breit-Wigner-like structure [51]. The PDG tables show that the mass and width of the σ are quite uncertain. Measurements of the mass range from 400 MeV to 1200 MeV, and the width from 200 MeV to 1 GeV.

Whether the σ actually exists as a short-lived particle is an important issue in QCD. The scalar mesons in the 1 GeV region constitute the Higgs sector of the strong interactions, and are responsible for the masses of all light flavor hadrons. The σ meson can be regarded as a fundamental feature of the QCD vacuum.

The ideal reaction to build an understanding of the σ is the $\gamma\gamma \rightarrow \pi\pi$ reaction. A recent partial wave analysis of the $\gamma\gamma \rightarrow \pi\pi$ cross sections found two distinct classes of solutions for the radiative widths of the scalar mesons [51]. New data with increased angular coverage and linear polarization are needed to constrain these analyses.

We have started to study rates, acceptances and resolution for a $\gamma\gamma \rightarrow \pi\pi$ measurement at JLab. The Primakoff cross section for two pion production is given by

$$\frac{d^2\sigma}{d\Omega dE_{\pi\pi}} = \frac{\alpha Z^2}{\pi^2}\sigma(E_{\pi\pi})\frac{\beta^2 E^4}{E_{\pi\pi}^2 Q^4}|F(Q)|^2 sin^2\theta_{\pi\pi}K_\pi$$

where $E_{\pi\pi}$ is the two pion invariant mass, K_π is the pion momentum in the two pion C.M. frame, and $\sigma(E_{\pi\pi})$ is the $\gamma\gamma \rightarrow \pi\pi$ cross section. Acceptable rates and acceptances for neutral pion production can be obtained by running at 11 GeV, but not at 6 GeV. This is because the cross section increases as E^4, and the photons have increased kinematic focusing at higher energies. A Hycal type detector was assumed for detecting the photons, with real photon tagging. We also believe that it will be important to have data with linear polarization to help constrain partial wave analyses of the data. Linearly polarized photons are currently available in Hall B, and are planned for Hall D. Work is continuing on the feasibility study for this experiment.

6 Summary

We have described a comprehensive program to measure the electromagnetic properties of pseudoscalar mesons which would be possible with advent of 11 GeV CW electron beams at Jefferson Lab. Precise measurements of the two photon widths and transition form factors would provide stringent tests of both QCD and QCD based models. We believe the proposed instrumentation to be constructed for this program will be of general use to both this program, and future experiments.

References

[1] F. Anulli, et al., p. 607 in Vol. II of The second $DA\Phi NE$

[2] A. Browman et al., Phys. Rev. Letts., vol. 33, no. 23, (1974)1400.

[3] J. Bijnens, A. Bramon and F. Cornet, Phys. Rev. Lett. 61 (1988) 1453.

[4] B. Moussallam, Phys. Rev. D51 (1995) 4939.

[5] E.P. Venugopal and B.R. Holstein, Phys. Rev D57 (1998) 4397.

[6] D. Haidt et al edit, Review of Particle Physics, Vol 3, (1998).

[7] H.J. Behrend, et, al., Z. Phys. C, 49 (1991) 401.

[8] M. Acciarri et al., Phys. Lett. B418 (1998) 399.

[9] J.F. Donoghue, E. Golowich, and B.R. Holstein, Dynamics of the Standard Model, Cambridge University Press (1992).

[10] J.S. Bell and R. Jaciw, Nuovo Cimento 60A (1969) 47; S.L. Adler, Phys. Rev. 177 (1969) 2426.

[11] International workshop on the structure of the η' meson, March 8–9, 1996, edited by M. Burkardt, J. Goity, V. Papavassiliou and S. Pate, World scientific.

[12] V.V. Anisovich et al, Phys.Lett.B404(1997)166.

[13] G. Bellettini et al., Il Nuovo Cimento, vol. 66, no. 1, (1970), 243.

[14] C.E. Hyde-Wright, W.Bertozzi and J.M. Finn, In Newport News 1985, Processdings, Continuous Electron Beam Accelerator Facility 532-551.

[15] R. Wilson, lecture given at Scottish University Summer School, T.W. Priest and L.L.J. Vick edit, Oliver and Boyd,1966.

[16] H. Enge, Nucl Inst and Meth 49(1967)181.

[17] S. Kowalski and H.A. Enge, RAYTRACE manual, 1987

[18] Ed V. Hungerford, L. Tang, R.E. Chrien, CEBAF proposal, E89009.

[19] A. Breskin, G. Charpak, S. Majewski, Nucl. Instr. and Meth. 220 (1984)349.

[20] K. Assamagan et al., Nucl. Instr. and Meth. A426(1999)405.

[21] L. Tang, A. Margaryan, TJNAF EXP95-002, Direct Measurement of the Lifetime of Heavy Hypernuclei at CEBAF.

[22] P. Degtyarenko, Experimental proposal for the determination of neutron spectra from targeted electron beam, JLAB - ACC - 96, 1996

[23] K. Pysz et al., Nucl. Instr. and Meth. A420 (1999) 356

[24] J. Drexler et al., Nucl. Instr. and Meth. 220 (1984) 409

[25] E.A. Arakelyan et al., Physics of Atomic Nuclei, v.58, n2(1995)219

[26] M. Overbeck et al., Nucl. Instr. and Meth. A288 (1990) 413

[27] M. J. M. van Sambeek et al., Nucl. Phys. A631 (1998) 545c

[28] M. J. M. van Sambeek et al., Nucl. Instr. and Meth. A434 (1999) 279.

[29] C. B. Fulmer, B.L. Cohen, Phys.Rev.,109 (1958) 94.

[30] P. Armbruster et al., Nucl. Instr. and Meth. 91(1971)499.

[31] Michael PAUL et al., Nucl. Instr. and Meth., A277 (1989) 418.

[32] K. Mengel, R. Novotny, R. Beck, *et al.*, "Detection of Monochromatic Photons Between 50 and 790 MeV with a $PbWO_4$ - Scintillator Array", to be published (1999).

[33] S.R. Amendolia et al., Phys. Lett. 146B (1984) 116.

[34] L.G. Landsberg, Phys. Rep. 128, no. 6 (1985) 302.

[35] R. Meijer Drees et al. Phys. Rev. D, Vol 45, no 5 (1992) 1439.

[36] F. Farzanpay et al., Phys. Lett. B278 (1992) 413.

[37] H. Fonvieille et al., Phys. Lett. B233 (1989) 65.

[38] P. Gumplinger, Doct. Thesis, Oregon State University (1987); J.M. Poutissou et al., Proc. Lake Louise Winter Institute (1987), World Scientific, Singapore.

[39] G. Tupper et al., Phys. Rev. D28, no 11 (1983) 2905.

[40] J. Fischer et al., Phys. Lett., Vol 73B, no. 3 (1978) 359.

[41] J. Burger, Doct. Thesis, Columbia University (1972).

[42] S. Devons et al., Phys. Rev., vol. 184, no. 5 (1969) 1356.

[43] N.P. Samios, Phys. Rev. Vol 121, no 1 (1961) 275.

[44] H. Kobrak, IL Nuovo Cimento, vol 20, no 6 (1961) 1115.

[45] E. Hadjimichael and S. Fallieros, Phys. Rev. C, vol. 39, no. 4 (1989) 1438.

[46] P. Maris and P.C. Tandy, Nulear physics A663&664 (2000) 401c.

[47] M.R. Frank, et al., Phys. Lett B359 (1995) 17.

[48] J. Bijnens, A. Bramon, F. Cornet, Z. Phys. C, 46 (1990) 599.

[49] D.M. Asner et al., CLEO CONF95-24, EPS0188, 1995

[50] D. Babusci et al., Phys. Lett. B 277, 158 (1992).

[51] M. Boglione and M.R. Pennington, Eur. Phys. J. C9 (1999) 11.

[52] J. Donoghue and B. Holstein, Phys. Rev. D, 48 (1993) 137.

[53] M. R. Pennington, "Riddle of the Scalars: Where is the σ?", unpublished.

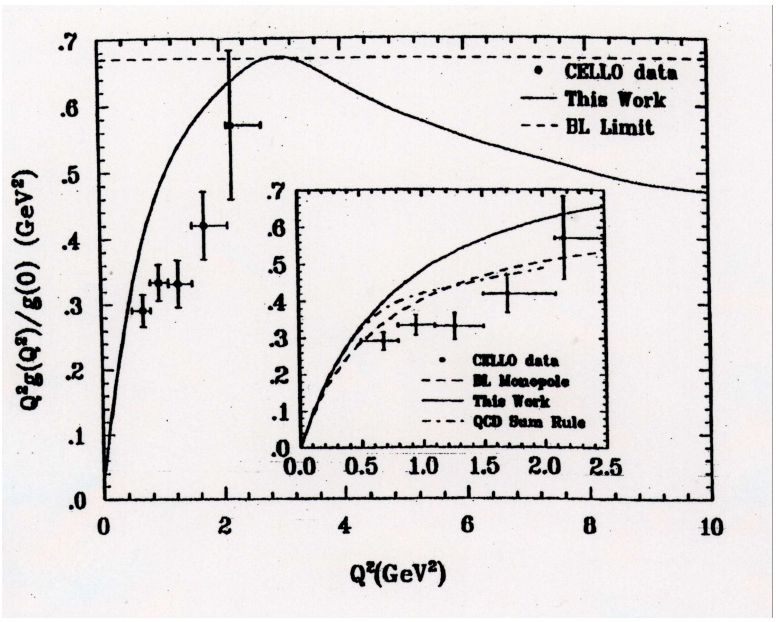

Figure 22: The $\gamma\gamma^*\pi^o$ form factor multiplied by Q^2. The data are from the CELLO Collaboration, and the solid line is the calculation of Frank. The dashed line is the pQCD factorization limit.

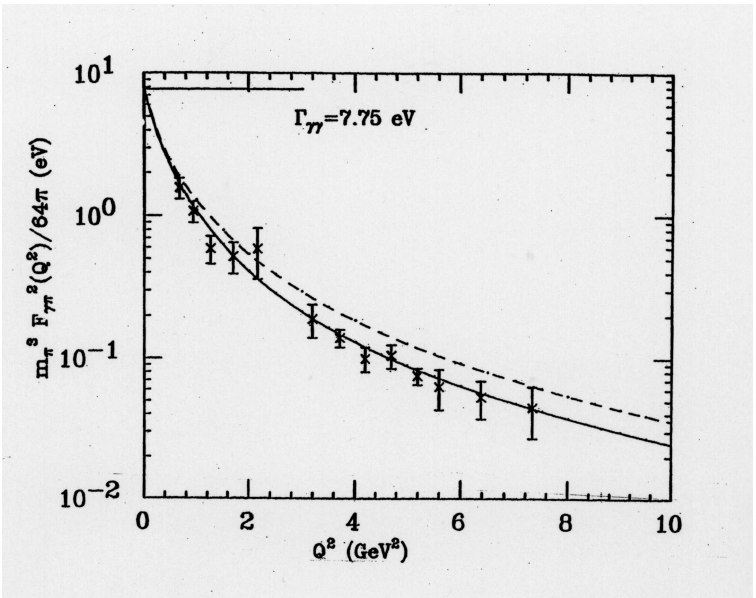

Figure 23: The $\gamma\gamma^*\pi^o$ form factor as calculated by Ivanov and Lyubovitskij. The data are from the CELLO and CLEO Collaborations.

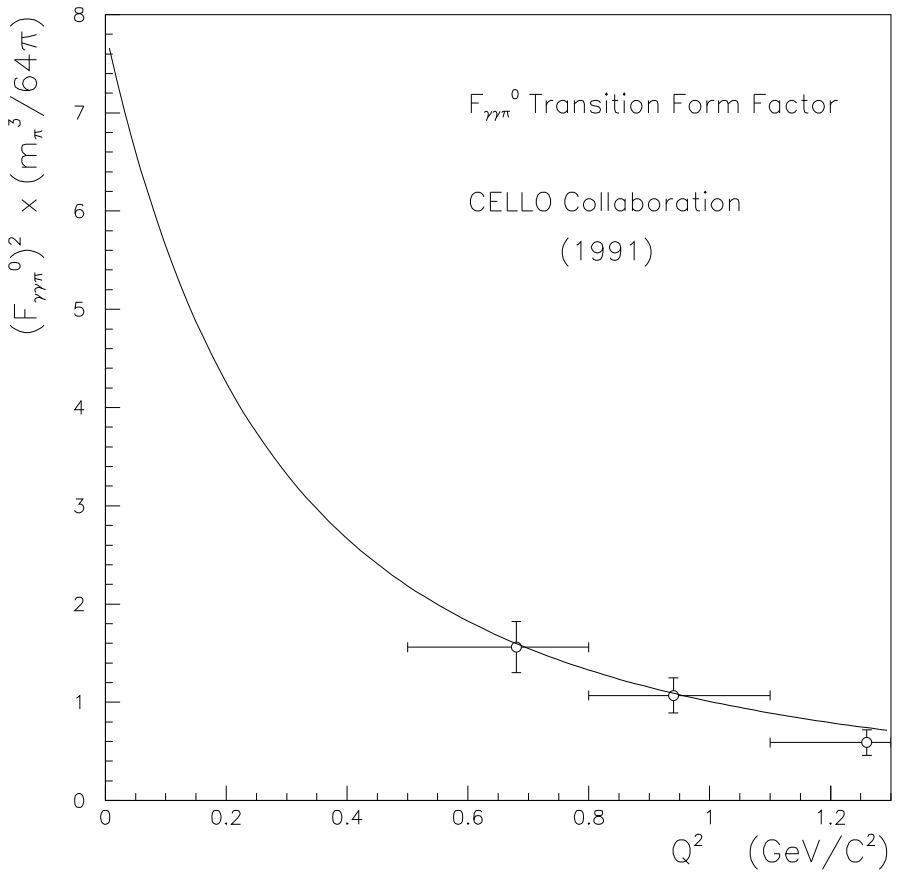

Figure 24: $F_{\gamma\gamma^*\pi^o}$ as measured by the CELLO Collaboration, with the low Q^2 extrapolation based on vector meson dominance.

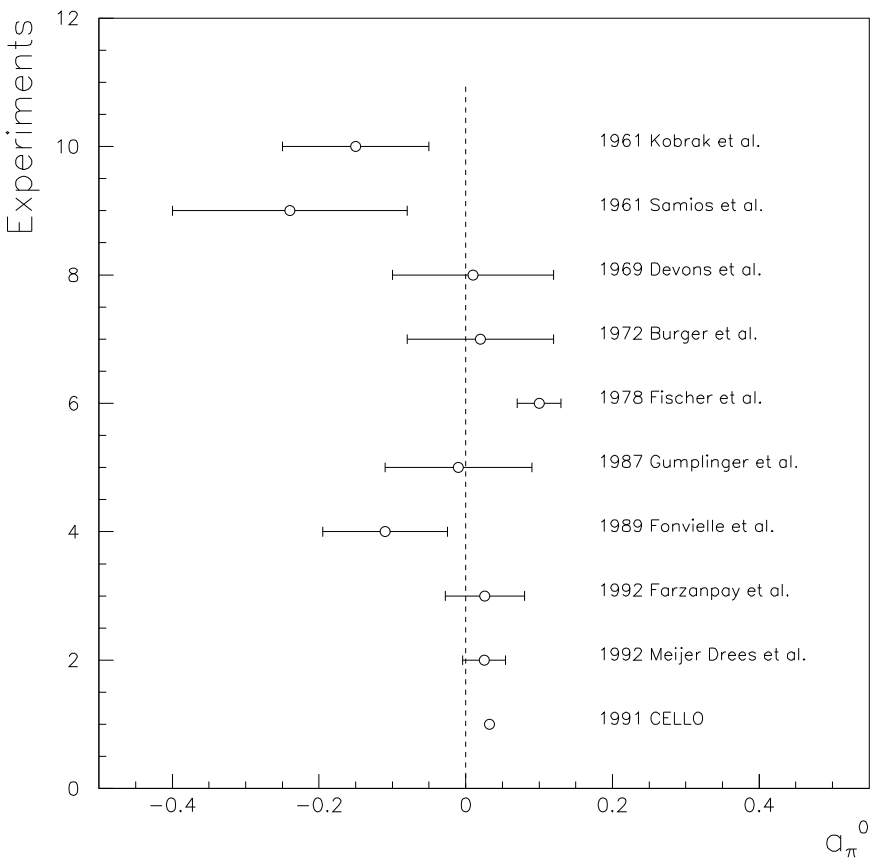

Figure 25: Summary of the previous slope measurements for π^0.

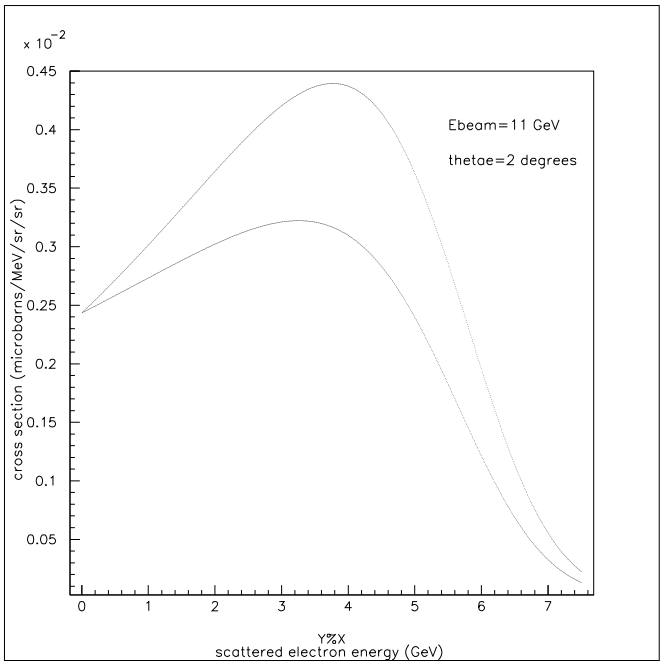

Figure 26: Cross section *verses* scattered electron energy for π^o production on helium-4. The incident electron energy is 11 GeV.

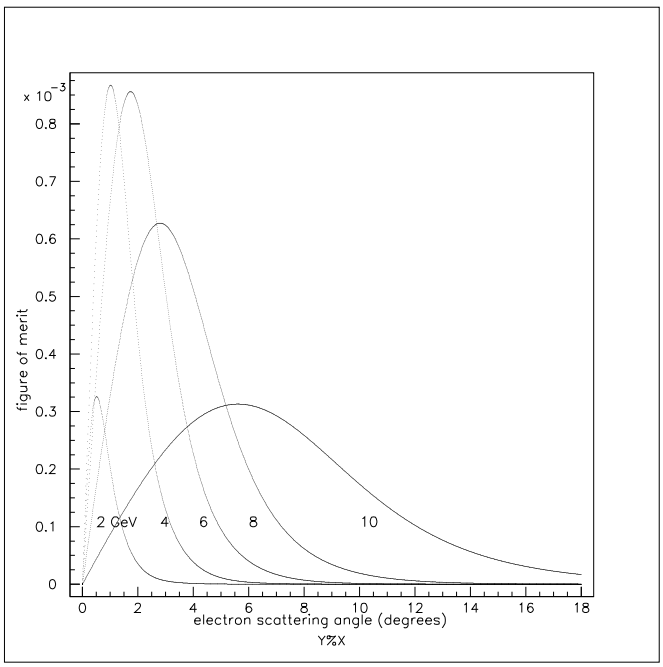

Figure 27: Figure of merit (see text) *verses* electron scattering angle for π^o production on helium-4. The incident electron energy is 11 GeV, and the various energy transfers are indicated.

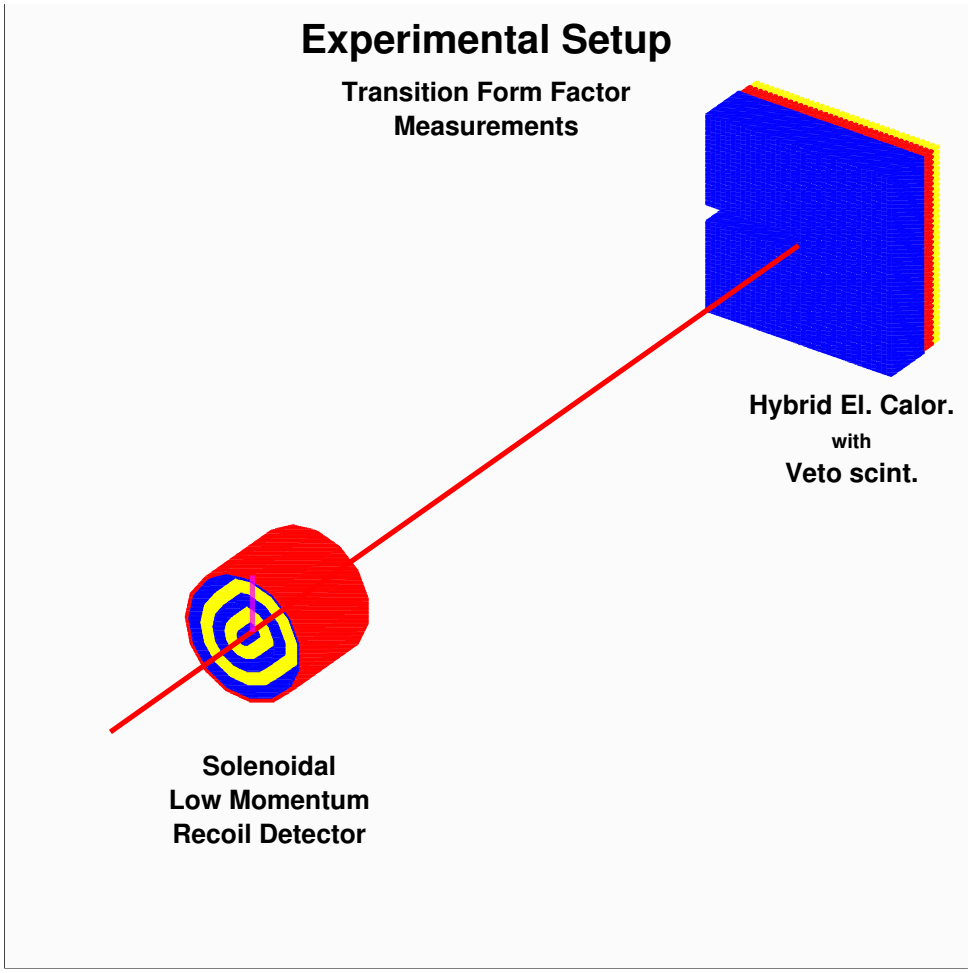
Experimental Setup
Transition Form Factor
Measurements
Hybrid El. Calor.
with
Veto scint.
Solenoidal
Low Momentum
Recoil Detector

Figure 28:

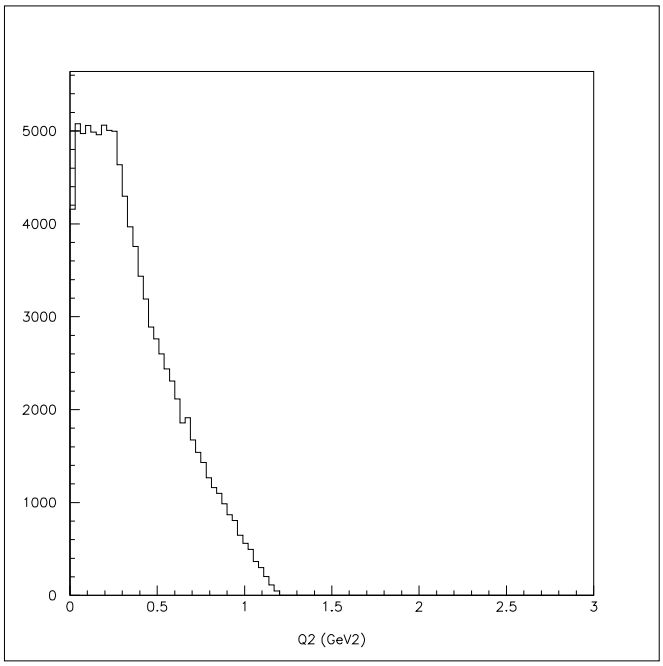

Figure 29: Phase space for Q^2 acceptance of a $1.5m \times 1.5m$ detector with a $12cm \times 12cm$ central hole. Detector is 7 m from target. Scattering angle is between 0.5 and 6 degrees. Energy transfer is between 2 and 10 GeV.

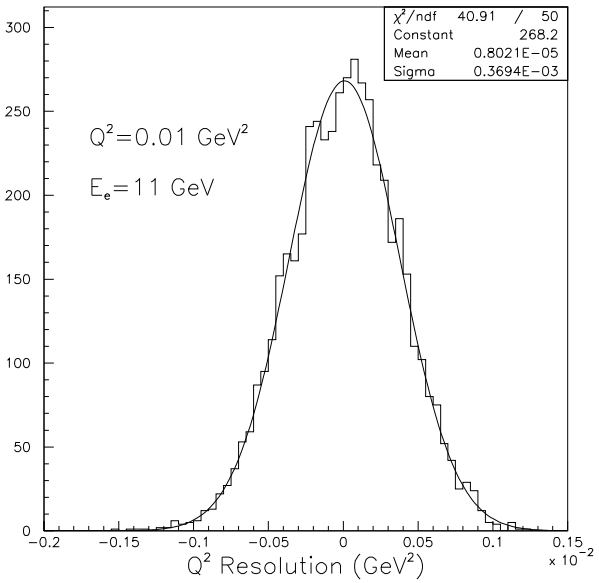

Figure 30: The difference in actual *verses* reconstructed Q^2 resolution for $Q^2 = 0.01 GeV^2$.

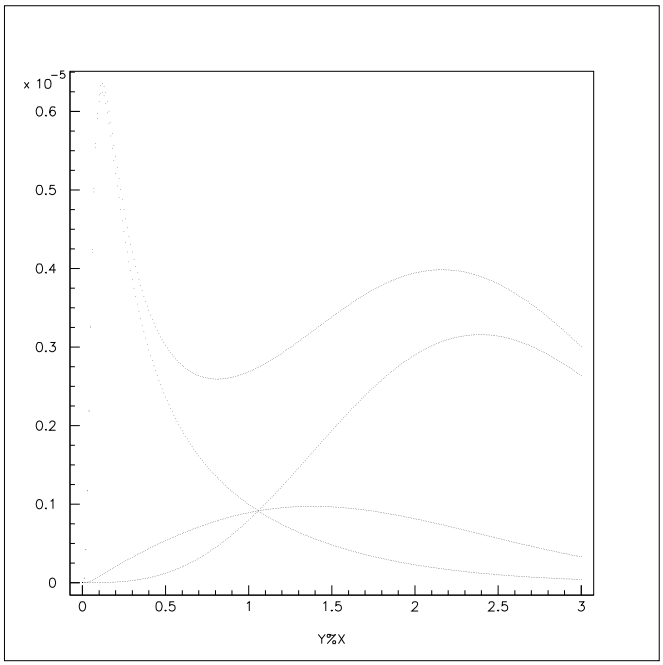

Figure 31: Cross section *versus* θ_π weighted by $sin(\theta_\pi)$ showing Primakoff, nuclear coherent, and their interference.

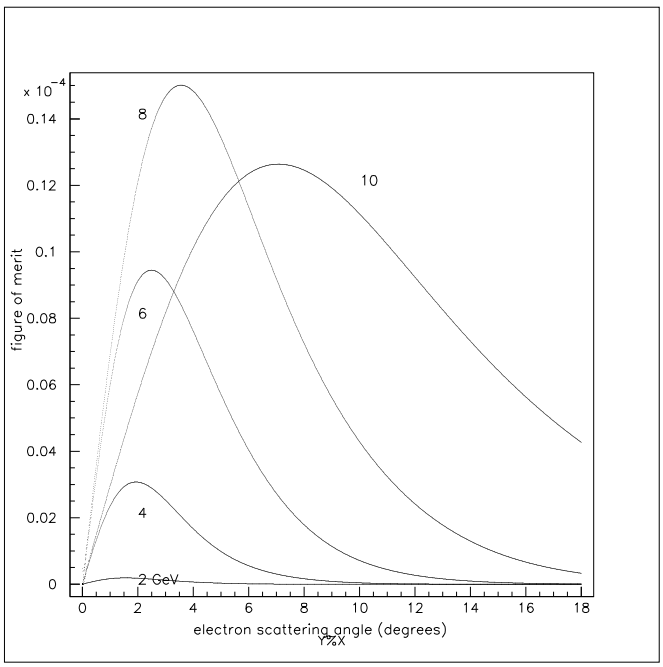

Figure 32: Figure of merit (see text) *verses* electron scattering angle for η production on helium-4. The incident electron energy is 11 GeV, and the various energy transfers are indicated.

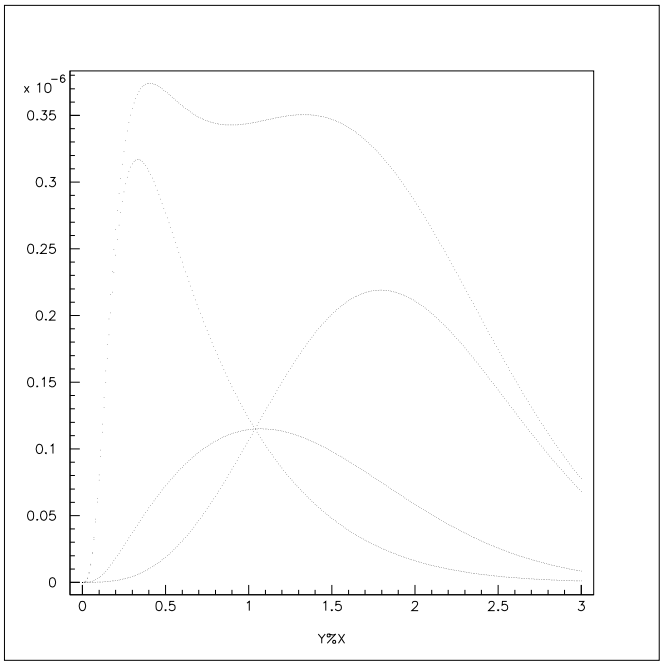

Figure 33: Cross section *versus* θ_η weighted by $sin(\theta_\pi)$ showing Primakoff, nuclear coherent, and their interference.

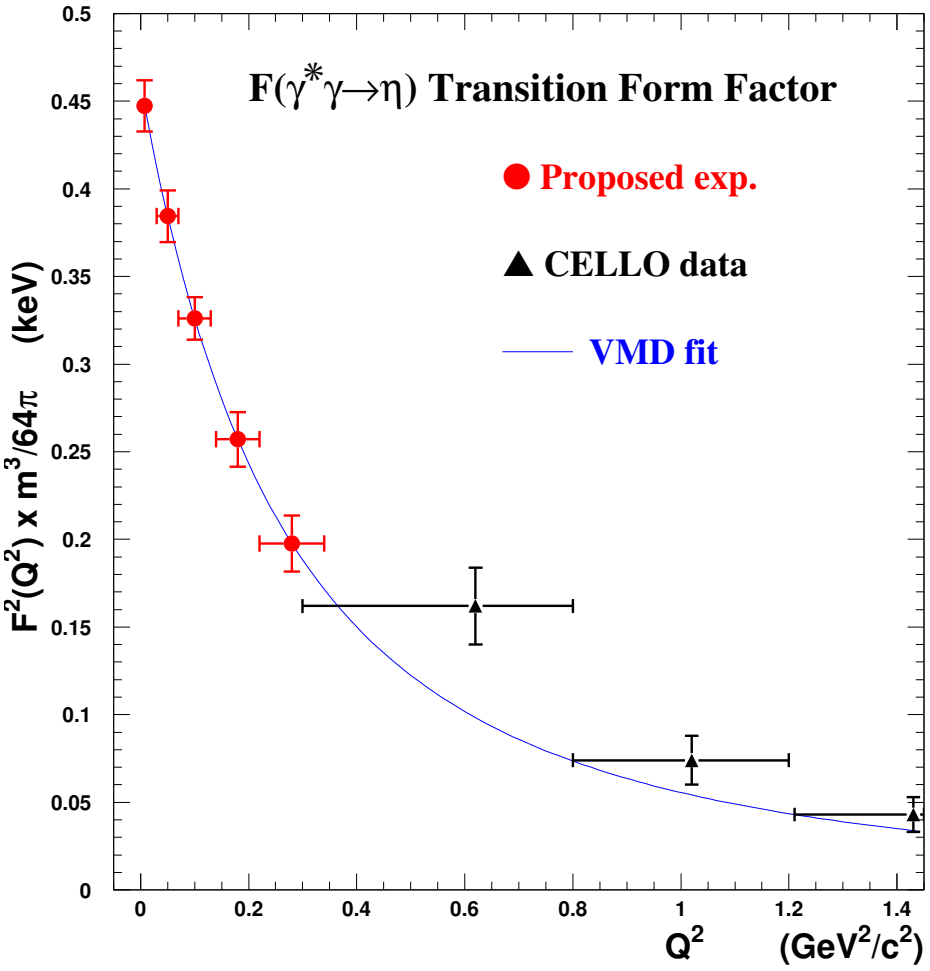

Figure 34: Monte Carlo simulation of η transition form factor on ^{12}C target. The proposed points are projected to the VMD prediction with expected total errors, in comparision with CELLO data[7].